NUMERICAL MODELLING AND OPTIMIZATION OF SOLAR NANOFLUIDS

by

Can Onur Akyüz

B.S., Mechanical Engineering, Istanbul Technical University, 2013

Submitted to the Institute for Graduate Studies in
Science and Engineering in partial fulfillment of
the requirements for the degree of
Master of Science

Graduate Program in Mechanical Engineering
Boğaziçi University

2017

NUMERICAL MODELLING AND OPTIMIZATION OF SOLAR NANOFLUIDS

APPROVED BY:

Assoc. Prof. Hakan Ertürk (Thesis Supervisor)	.....
Assoc. Prof. Hasan Bedir	.....
Assist. Prof. Altuğ Melik Başol	.....

DATE OF APPROVAL: 06.01.2017

ABSTRACT

NUMERICAL MODELLING AND OPTIMIZATION OF SOLAR NANOFLUIDS

Direct Absorption Solar Collectors (DASCs) have gained popularity as a new and promising design for solar collector systems. DASCs utilize nanofluids to absorb solar energy directly; eliminating the need for an absorber tube, and providing increased efficiency. Nanofluids are dilute suspensions with dispersed nano-sized particles that show good thermal and optical or radiative properties. This study focuses on optimizing the overall system efficiency of a flat plate collector system using nanofluids. Core shell and pure nanoparticles are considered along with water and ethylene glycol as base fluids. Core-shell nanoparticles are spherical particles with multiple layers of different materials that can be selected for optimal absorption characteristics. The collector model considers direct absorption of solar energy by a flowing nanofluid, while the spectral radiative properties of the nanofluid are predicted based on Lorenz-Mie theory. Different volume fraction, particle size and shell thickness values are considered for each nanofluid type, and optimal parameters are determined.

ÖZET

GÜNEŞ ENERJİSİ İÇİN KULLANILAN NANOAKIŞKANLARIN SAYISAL MODELLEMESİ VE OPTİMİZASYONU

Doğrudan Soğurmalı Güneş Kollektörleri (DSGK), yeni ve gelecek vaat eden bir güneş enerjisi dizaynı olarak dikkat çekmektedir. DSGK'lar nano-akışkanlar yardımıyla güneş enerjisini doğrudan soğurarak ek bir soğurucu tüpe ihtiyacı ortadan kaldırır ve verimliliği artırırlar. Nano-akışkanlar, nano boyutta parçaçıkların içinde çözündükleri seyreltik süspansiyonlardır ve iyi ısısal ve optik özellikler sergilerlerler. Bu çalışma düz plaka güneş enerjisi kollektörlerde nano-akışkan kullanımının optimizasyonunu amaçlamaktadır. Çekirdek-Kabuk ve saf nano-parçacıklar ile beraber baz sıvı olarak su ve etilen glikol araştırmaya dahil edilmiştir. Çekirdek-Kabuk nano-parçacıklar bir veya birden fazla katmanı olabilen küresel parçacıklardır. Bu parçacıkların boyutları ve malzemeleri güneş ışığını soğurma özelliklerini azami duruma getirecek şekilde seçilebilir. Kollektör modeli güneş enerjisinin nano-akışkan tarafından direk olarak soğurulması temeline dayanır ve nano-akışkanın dalga boyutuna bağlı ışınım özellikleri Lorenz-Mie Teorisi ile hesaplanır. Farklı konsantrasyon, parçacık boyutu ve kabuk kalınlığı değerleri her nano-akışkan için ayrı değerlendirilip optimal parametreler belirlenmesi bu çalışmanın ana amacıdır.

TABLE OF CONTENTS

LIST OF FIGURES

LIST OF SYMBOLS

A	Fitting parameter, constant for thermal conductivity model
abs	Absorption
bf	Base fluid
B	Constant used in thermal conductivity model
C	Concentration ratio
C_a	Scattering cross section
C_e	Extinction cross section
C_s	Scattering cross section
c	Speed of light
c_p	Specific heat capacity
eff	Effective
F_d	Forward to backward scattering ratio
f_v	Volume fraction
G	Incident intensity
G_i	Incident solar intensity
g	Asymmetry parameter
H	Receiver depth
I	Intensity
I^+	Upper hemispherical intensity
I^-	Lower hemispherical intensity
I_b	Blackbody intensity
k_b	Boltzmann's constant
k	Thermal conductivity, imaginary part of the complex index of refraction
l	Mean free path
m	Relative complex index of refraction
N	Radiation conduction parameter
Nu	Nusselt number
n	Real Part of the complex index of refraction

nf	Nanofluid
np	Nanoparticle
Q	Heat
Q_a	Absorption efficiency
Q_e	Extinction efficiency
Q_s	Scattering efficiency
$\dot{q}$	Local energy source
q_c	Convective heat flux
q_r	Radiative heat flux
q_r^+	Upper hemispherical radiative heat flux
q_r^-	Lower hemispherical radiative heat flux
r	Radius
$\tilde{r}$	Complex reflection coefficient
S	Coordinate along path of radiation
T	Temperature
T_b	Bulk temperature
t	Time
tot	Total
$\tilde{t}$	Complex transmission coefficient
U	Velocity
v_f	Fermi velocity
α	Absorptivity
β	Extinction coefficient, thermal expansion coefficient
γ	Relaxation frequency
δ	Ratio of shell radius to core radius
ε	Emissivity
ϵ	Dielectric function
ϵ_1	Real part of the complex dielectric function
ϵ_2	Imaginary part of the complex dielectric function
ϵ_{rel}	Relative error

ζ	Non-dimensional axial length
η	Efficiency
η_0	Wavenumber
κ	Absorption coefficient
θ	Angle of incidence
λ	Wavelength, spectral quantity
μ	Viscosity, cosine of angle
ν	Non-dimensional height
κ	Absorption coefficient
ξ	Size parameter
ρ	Density, reflectivity
$\rho_{nf\rightarrow a}$	Reflectivity of glass cover from nanofluid to air
σ	Stefan-Boltzmann constant
σ_s	Scattering coefficient
$\tau_{a\rightarrow nf}$	Transmissivity of glass cover from air to nanofluid
τ_d	Optical thickness
Φ	Scattering phase function
Φ_d	Energy generation due to viscous dissipation
χ	Angle of refraction
Ω	Solid angle
Ω_i	Incident solid angle
ω	Scattering albedo, circular frequency
$\omega_{bound,j}$	Resonance frequency of the jth oscillator
ω_p	Plasma frequency

LIST OF ACRONYMS/ABBREVIATIONS

2D	Two Dimensional
3D	Three Dimensional
CPV	Concentrated Photovoltaic
CSP	Concentrating Solar Power
DASC	Direct Absorption Solar Collector
DSSC	Dye Sensitized Solar Cell
EG	Ethylene Glycol
GOA	Geometric Optic Approximation
HG	Henyey-Greenstein
HTF	Heat Transfer Fluid
LFR	Linear Fresnel Reflector
LMT	Lorenz-Mie Theory
NP	Nanoparticle
PDC	Parabolic Dish Collector
PTC	Parabolic Trough Collector
PV	Photovoltaic
PVT	Photovoltaic/Thermal
PVSP	Photovoltaic Solar Panel
RSA	Rayleigh Scattering Approximation
RTE	Radiative Transfer Equation

1. INTRODUCTION

1.1. Motivation

Today's world is highly dependent on energy, for industrial and domestic use. The energy demand is projected to increase in the near future as seen in Figure 1.1. Fossil fuels were the predominant source of energy until the mid-twentieth century. However in the second half of the twentieth century two main concerns have been raised in regards to fossil fuels: that their excessive use can be harmful, and heavy dependence on them can cause significant problems in the future due to limited supply. The main cause for concern regarding nature is the greenhouse effect due to by-products of the energy produced by fossil fuels, which accumulate in the atmosphere and cause climate change [1]. Use of fossil fuels also cause significant air pollution threatening humans and wildlife. The second concern is the fact that the world economy has been based on the use of energy derived mainly from fossil fuels, and future shortage of such a resource must be considered, and precautions must be taken for this eventuality.

Figure 1.1. World energy consumption [2].

The major alternatives to replace fossil fuels are nuclear and renewable energy. Nuclear energy has risks due to the possibility of accidents that have even more devastating effects. Countries such as Germany, Switzerland and Japan have begun to phase-out nuclear power due mainly to safety concerns. This leaves renewable energy sources as the only viable alternative to become the main energy source of the future.

Wind power, hydro-power, and solar energy are the main renewable energy sources that have the capacity to replace the use of fossil fuel or nuclear energy. Among them, solar energy can be used in a much wider geographical area, including regions where either wind regimes are not stable or adequate enough to sustain yearlong energy production or where there is no available hydrological power source.

1.2. Solar Energy Systems

Solar energy can be utilized mainly by two methods: using photovoltaic effect to generate electricity directly, or by solar thermal systems to heat working fluids, which are then used in a thermodynamic power cycle to produce electricity.

Photovoltaic principle is used in Photovoltaic Solar Panels (PVSP), Dye Sensitized Solar Cells (DSSC), and Concentrated Photovoltaic Systems (CPV). They are built as an array of cells for PV and DSSC systems [3].PVSPs utilize semiconductors that show photovoltaic characteristics. Materials that exhibit such behavior and that are being actively used are mono- and polycrystalline silicon, amorphous silicon, cadmium telluride and copper indium gallium selenide/sulfide. The working principle is as follows. The semiconductor material absorbs incident photons due to solar radiation. These photons have different energy levels that correspond to the overall solar spectrum. Photons that are above the "band-gap energy", which is different for each material, free electrons from their covalent bonds, allowing them to be used in generating direct current electricity. Energy left over after the electron is freed turns into kinetic energy of the electron and causes heating. The excess energy that becomes heat is an important design consideration that affects both efficiency and durability of the system. Efficiency values for a typical solar cell range from 15% to 17.2% [4].

Photovoltaic Solar Panels are flat panels that are composed of an array of solar cells. They are the most commonly used method for harvesting solar energy [5].

Dye Sensitized Solar Cells (DSSCs), are made up of a photosensitized anode and an electrolyte, which act together as a semiconductor. Their uniqueness comes from the fact that they use photosensitive dyes (most commonly used are ruthenium-based molecular dyes) to coat a film of TiO_2 or ZnO particles. These films have a thickness on the order of micrometers [6]. The main setback of DSSCs are that the liquid electrolytes that used become unstable at high temperatures, and are volatile. This has slowed down the commercialization of DSSCs and there is ongoing research into the replacement of these electrolytes with reliable alternatives [7].

Concentrated Photovoltaic (CPV) systems' main difference from PVSPs and DSSCs is that reflective panels are used for CPV systems to concentrate incident solar radiation to the photovoltaic unit. These systems allow for much lower production costs compared to PVSPs, because CPVs require considerably less semi-conductor material.

For solar power systems to become a viable alternative to replace conventional energy sources, they must also be able to supply useful work during night-time or when sunlight is not available due to weather conditions such as clouds. Therefore for systems utilizing the photovoltaic technology another auxiliary system must be coupled that potentially decreases overall efficiency and increases overall investment costs. However, in Concentrated Solar Power (CSP) systems, the incident solar radiation is concentrated to heat the working fluid and the thermal energy transferred to working fluid can be stored for continuous production of useful work. Besides, CSP systems can also be coupled with conventional fuel systems either for backup or night-time use [8].

The CSP systems can be used employing various designs; the most widely used designs are Solar Power Towers (SPT), Linear Fresnel Reflectors (LFR), Parabolic Dish Collectors (PDC), and Parabolic Trough Collectors (PTC). The most commonly used design is the PTS as can be seen in Figure 1.2.

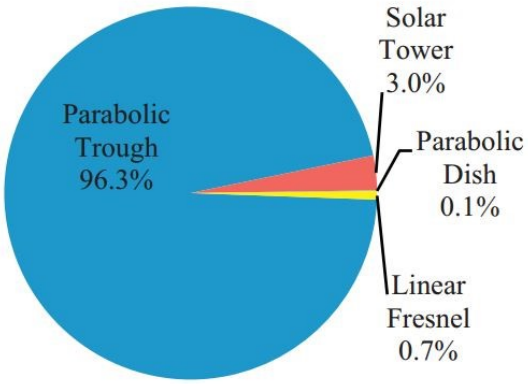

Figure 1.2. Installed and Operational CSP technology [9].

Solar Power Tower systems comprise of a central receiver and a heliostat field collector. Heliostats are reflectors that track the suns position and reflect the sunlight to the central receiver placed in a tower. Heliostats can be either flat or concave mirrors, and the central receiver contains a heat transfer fluid (HTF) heated by the incident concentrated solar energy and used in a heat engine. While there are systems that make use of direct steam generation, as the HTF might reach very high temperatures due to the high concentration of solar radiation, different types of fluids have been utilized as HTFs, such as molten salts, that can also be effectively used as thermal storage media. Another type of CSP system is the Linear Fresnel Reflector (LFR) that consists of long rows of either flat or slightly curved mirrors reflecting the incident sunlight to a central receiver located upon a tower. Linear Fresnel Reflector plants have simple design and relatively lower investment costs; however, they are less efficient compared to PTCs [9]. Parabolic Dish Collectors (PDC) concentrate the incident sunlight to a receiver at an intensity up to 1000 times the intensity of solar flux. While this can result in temperatures above 1500°C at the receiver, the heat energy gathered by the receiver is used by a heat engine which in turn generates electricity. Downsides of the PDCs are their relatively high cost, and difficulty of coupling them to thermal energy storage systems. Parabolic Dish Collectors also have much lower power production capacity per each unit; therefore, a large number of PDCs must be utilized for high output power plants [10].

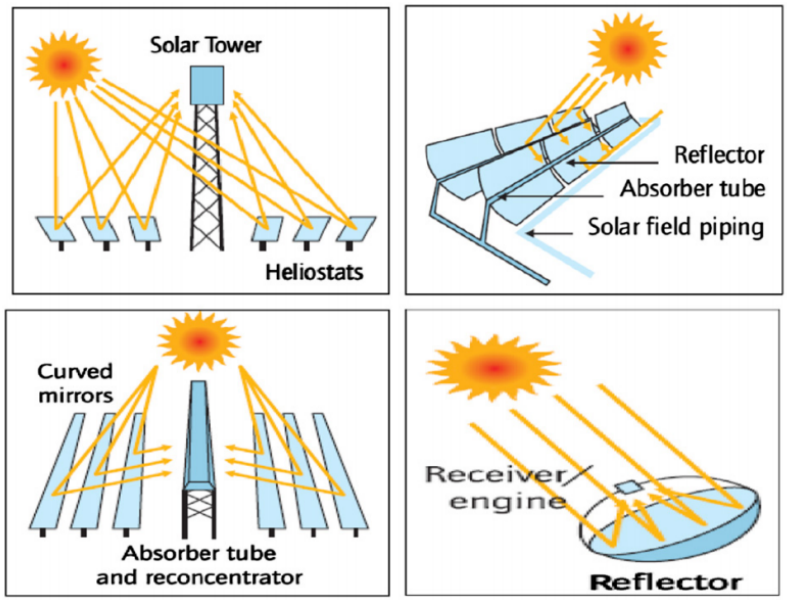

Figure 1.3. Types of CSP systems from top left clockwise: SPT, PTC, LFR, and PDC [9].

The final type of CSP system that is frequently used is the Parabolic Trough Collector (PTC). While the PTC is the most common and mature CSP technology, further developments in regards to PTC's are still an active research field. Parabolic Trough Collectors consist of mirrors that are generally made of silvered acrylic and curved in a parabolic shape, and an absorber tube placed at the focal point of the reflectors. Thermal oils are the most commonly used heat transfer fluid, but there are also applications that utilize molten salts or direct steam generation systems. Tracking systems are used to maximize solar absorption and the HTF in the absorber tube can reach temperatures up to 400°C [11].

An important component of conventional PTC systems is the absorber tube. The HTF flows inside the absorber tube and is heated by the concentrated sunlight coming reflected from the parabolic mirrors. Most commonly used HTFs are synthetic oils such as Biphenyl-diphenyloxide, also known as Therminol VP-1, water and molten salts. Specially coated absorber tubes are designed to absorb the concentrated solar energy and transfer it to the HTF via conduction and convection.While the coating maximizes

the absorption of solar energy, it minimizes the heat loss by emission. Metal tubes are used as absorber tubes and they are enclosed in a glass envelope with vacuum between the absorber and the glass to minimize convection heat loss to environment [12].

There are also non-concentrating solar collectors, which are mainly used in low temperature applications. Applications include water heating and space heating [13]. These are conventional flat plate, photovoltaic flat plate, hybrid photovoltaic/thermal (PVT) flat plate and bifacial PVT flat plate collectors [14]. Photovoltaic (PV) flat plate collectors utilize the photovoltaic effect whereas hybrid PVT systems also capture the heat generated by the PV system. This is accomplished by attaching an absorber plate to the back of the PV component, which simultaneously cools it and heats a working fluid flowing underneath. This leads to an increased efficiency compared to that of the PV flat plate system. Bifacial PVT collector is a new concept proposed by Tina *et al.* [15] comprises a solar panel submerged in water. This reduced losses due to reflection and provided better cooling for the PV module. Conventional flat plate collectors do not use a PV system, relying on an absorbing plate to absorb solar radiation and transfer it to the working fluid. Conventional flat plate collectors have the advantage of lower initial and maintenance costs and technological maturity.

1.3. Nanofluids

A new type of solar energy system design has emerged with the introduction of nanofluids. With this design, called Direct Absorption Solar Collector (DASC), sunlight is absorbed directly by the nanofluid used as the HTF, eliminating the need for an absorber tube [16].

This design was made possible by the unusual properties of nanofluids. Nanofluids are suspensions of nanoparticles with water, oils or glycols as base fluids. Particle sizes are usually in the range of 1 to 100 nanometers and volume fractions differ depending on the application. They were first put forth in 1995 by Choi [17]. The applications of nanofluids include microelectronics, pharmaceutical processes, fuel-cells and optics, and lubrication. Nanofluids show increased thermal conductivity [18], convective heat

transfer properties [19,20] and much better optical properties compared to conventional HTFs used in PTC systems [21].

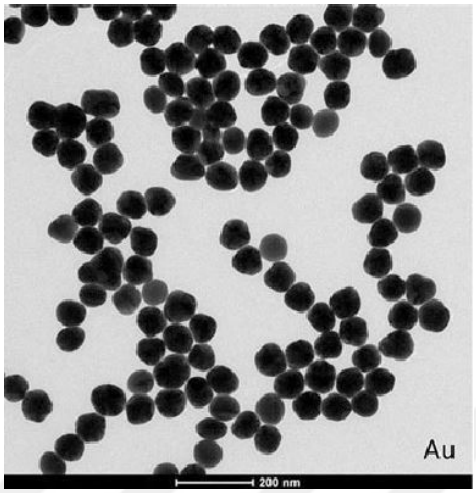

Figure 1.4. TEM image of nanofluid with gold nanoparticles [22].

1.4. Literature Survey

Research has been conducted regarding the possibility of replacing conventional HTFs with nanofluids. The most important property of nanofluids considered for use in DASCs is their ability to absorb a significant amount of incident solar radiation. This property can be quantified by the nanofluid's extinction coefficient. Extinction coefficient is the sum of absorption coefficient and scattering coefficient, and is a measure of how much the electromagnetic radiation is attenuated inside the medium.

The extinction coefficient values of nanofluids have been investigated by Taylor *et al.* [23] both experimentally and numerically. Nanoparticles used were copper, titanium-oxide, graphite, aluminium, gold and silver with different volume fractions. The two models used were independent mode Rayleigh scattering and Maxwell-Garnett effective medium models. These models have under-predicted the experimental results, but captured the general trend of the extinction coefficients.

Moreira *et al.* [24] investigated thermal and optical properties of silver and gold nanofluids by obtaining the extinction coefficient of both nanofluids experimentally. A numerical model using Lorenz-Mie theory was developed to find out the mean particle size of the nanofluids by fitting the data with numerical results.

Otanicar *et al.* [25] studied numerically the impact of size and scattering mode of nanofluids for use in solar applications. The results showed that the size of the nanoparticles can be adjusted in order to increase the amount of solar absorption, decrease thermal emission, and maximize efficiency. Mercatelli *et al.* [26] worked on absorption and scattering properties of nanofluids with single wall carbon nanohorns as nanoparticles and water and glycol as base fluids. Their results showed that use of nanohorns in DASCs is possible. In [27], optical properties and the spectral scattering albedo of the nanohorn-based nanofluid was experimentally and numerically investigated. Results of the Rayleigh-scattering-based numerical model was in accordance with experimental data.

There has also been research into numerical modelling of DASC systems using nanofluids. Khullar *et al.* [28] developed a numerical model to study the application of nanofluids within DASCs with a finite difference scheme using radial discretization, with radiation boundary conditions obtained from radiative transport equation. Results were compared with experimental data from conventional PTCs and higher efficiency values(5% to 10%) were reported. In [29], the radiative heat transfer equation was solved using the Schuster-Scwarzschild approximation, considering the scattering properties of nanoparticles in the fluid. They compared the performance of a conventional collector and nanofluid-based collectors, and validated their predictions with data from an experimental micro-collector that they built. They reported that nanofluid-based collectors improved efficiency by up to 25%, and that nanoparticle material had considerable effect on solar absorption qualities of the nanofluid. Another numerical study was carried out by Tyagi *et al.* [30] to evaluate the applicability of DASC concept for low temperature applications using a two-dimensional flow model coupled with radiative transport equation. Nanofluid DASC outperformed conventional flat plate collector with an efficiency increase of up to 10%. Increased volume

fraction, collector depth, and glass-cover transmissivity improved collector efficiency.

Molten salt nanofluids were also considered for solar energy applications. Molten salt performance for a conventional PTC system was compared by Kearney *et al.* [31] with Therminol VP-1, a heat transfer fluid used in state-of-the-art PTC systems. Their parametric study showed that molten salts can achieve higher efficiency levels due to high operating temperatures and lower pressure losses. It was noted that higher temperatures would increase thermal losses and the high freezing point of molten salts (ca. 120°C) would necessitate using some of the energy gained to be used in freeze-protection. Drotning [32] experimentally investigated the absorption properties of two nanofluids with Hitec molten salt as base fluid and Co_3O_4 and CuO as nanoparticles. Addition of nanoparticles were shown to increase absorption properties from 8% up to 90 %. It was also found that forward scattering of the nanoparticles required hemispherical detection techniques. Finally, temperature dependence of the absorption coefficients were determined to be negligible. Tyagi *et al.* [33] studied numerically a nanofluid with a mixture of two molten salts (Na_2CO_3 and K_2CO_3) as the base fluid together with copper nanoparticles, for use in conversion of biomass to fuel. They showed that such a system was viable and performance increased with higher concentration ratios. Due to the elimination of an intermediary heat transfer step with direct absorption, the proposed method was determined to be more efficient than conventional systems.

Scaffardi and Tocho [34] conducted a numerical study on the size dependence of the refractive index of gold nanoparticles. They showed that Lorenz-Mie theory solutions can accurately obtain the extinction coefficient for gold nanoparticles if appropriate modifications to the dielectric function are made. Another result emphasized was the need to modify the bound electron contribution to the dielectric function to obtain accurate results.

Core-Shell nanoparticles were another type of nanoparticle proposed for use in DASC systems. Core-shell nanoparticles are spherical particles made up of two different materials. They provide the opportunity to use combinations of different materials to

enhance thermo-physical and optical characteristics of the nanofluids. Blaber *et al.* [35] investigated nanoshells with an empty core and various shell materials comprising aluminium, sodium, gold, silver and potassium for optimal absorption efficiency. Their numerical study has shown that size and shell thickness values for maximum efficiency are considerably different for modified and non-modified dielectric functions and surface scattering must be included for an accurate model of core-shell nanoparticle optical properties. Lv *et al.* [36] conducted a numerical investigation of the effect of core and shell materials and radii on the optical properties of the nanofluid. Silica was chosen as the core material along with gold, silver, copper and aluminum for the shell. A comparison of solar absorption characteristics was considered for different ratios of core and shell sizes to obtain the best geometry. The study reported that silica core metallic shell nanoparticles offered the same solar absorption efficiency as their purely metallic counterparts, which could lead to significant cost reduction. Lee *et al.* [37] proposed blended core-shell nanofluids made of different sized nanoparticles. The size dependence of the plasmonic peaks was used in broadening the absorption band of the nanofluid. The analysis was expanded with a two-dimensional steady-state model of the flow, which showed improved efficiency even at very low particle concentrations.

1.5. Objective of Study

Although the optical properties of core-shell nanoparticles have been studied, a combined thermal model investigating the thermal performance of core-shell nanofluids that also incorporates their scattering behavior has not been considered for DASC. The aim of this study is to investigate the combined optical and thermal properties of core-shell and pure nanofluids in DASC systems. The collector is approximated as a two-dimensional plane parallel system and the coupled radiative transfer and energy equations must be solved simultaneously. The optical properties of nanoparticles are obtained using the Lorenz-Mie Theory, which is suitable for the detailed characterization of absorption and scattering properties of nanoparticles. This allows the use of a wide range of nanoparticle sizes. Two-Flux approximation is employed for solution of radiative transfer equation in order to include scattering due to nanoparticles. The

impact of shell thickness is also analysed to determine its influence on the performance of the system. The effects of volume fraction and nanoparticle material are also taken into account. Since carbon-based nanofluids are also suitable for solar applications, graphite nanoparticles are included in the study, so as to compare their performance to metal-based pure and core-shell nanofluids.

2. THEORETICAL MODEL

2.1. Overview

The problem requires simultaneous solution of two coupled equations: radiative transfer equation (RTE) and energy balance equation. The differential form of the RTE is [38]:

$$\frac{\partial I_\lambda(S,\Omega,t)}{\partial S} = \kappa_\lambda I_{b,\lambda}(S,t) - \kappa_\lambda I_\lambda(S,\Omega,t) - \sigma_{s,\lambda} I_\lambda(S,\Omega,t) + \frac{1}{4\pi}\int_{\Omega_i=4\pi} \sigma_{s,\lambda} I_\lambda(S,\Omega_i,t)\Phi_\lambda(\Omega_i,\Omega)d\Omega_i \tag{2.1}$$

here S is the coordinate along path of radiation, Ω is the solid angle, t is time, λ is the wavelength, I_λ and $I_{b,\lambda}$ are spectral intensity and spectral blackbody intensity, Ω_i is the incident solid angle, κ_λ and σ_λ are the spectral absorption and scattering coefficients and Φ_λ is the spectral scattering phase function. The term on the left side represents the change in radiative energy whereas the terms on the right hand side are, respectively, energy gain due to emission, loss due to absorption, loss due to out-scattering and gain due to in-scattering. The RTE is an integro-differential equation and as such a full analytic solution is not obtainable. Therefore, this equation must either be solved numerically in its full form, which can be computationally demanding, or certain assumptions must be made that suits the problem at hand in order to simplify it. One obtains the spectral intensity I_λ by solving the RTE. This intensity term is used to obtain the divergence of the radiative heat flux [38]:

$$-\nabla \cdot \mathbf{q}_r = \int_{\lambda=0}^{\infty} \kappa_\lambda \left[\int_{\Omega_i=0}^{4\pi} I_\lambda(\Omega_i) d\Omega_i \right] d\lambda - 4\pi \int_{\lambda=0}^{\infty} \kappa_\lambda I_{\lambda,b} d\lambda \tag{2.2}$$

This expression is then used in the energy conservation equation to solve for the temperature distribution:

$$\rho c_p \frac{DT}{Dt} = \beta T \frac{DP}{Dt} + \nabla \cdot (k\nabla T - \mathbf{q}_r) + \dot{q} + \Phi_d \tag{2.3}$$

where D/Dt is the material derivative, ρ and c_p is the density and specific heat capacity of the material, β is the thermal expansion coefficient, P is pressure, k is the thermal conductivity, T is the temperature, $\dot{q}$ is the local energy source, and Φ_d is energy production by viscous dissipation. Using the divergence of heat flux, the temperature profile can then be acquired using Equation 2.3.

2.2. Radiation Model

Taking into account the geometry and characteristics of the physical system, the Two-Flux approximation method was used to simplify Equation 2.1. This method assumes steady state and 1-D geometry for the RTE. Equation 2.1 simplifies considerably when diffuse radiation and azimuthal symmetry is assumed. Using a change of variables $\mu = cos\theta$ and employing the main assumptions stated above, one obtains [39]:

$$\mu \frac{dI_\lambda}{dy} = -(\kappa_\lambda + \sigma_{s,\lambda}) I_\lambda(\mu) + \kappa_\lambda I_{\lambda,b} + \sigma_{s,\lambda} \int_{-1}^{1} I_\lambda \Phi(\mu') d\mu' \tag{2.4}$$

The Two-Flux Model approximates the intensity I_λ as a combination of upper and lower hemisphere components I_λ^+, and I_λ^- with the relation:

$$I_\lambda = I_\lambda^+ - I_\lambda^- \tag{2.5}$$

Using this relation and integrating over the forward and backward hemispheres results in two coupled ordinary differential equations:

$$\frac{1}{2}\frac{dI_\lambda^+}{dy} = -(\kappa_\lambda - \sigma_{s,\lambda} F_d) I_\lambda^+ + \sigma_{s,\lambda}(1 - F_d) I_\lambda^- + \kappa_\lambda I_{b,\lambda}(T(y)) \tag{2.6}$$

$$-\frac{1}{2}\frac{dI_\lambda^-}{dy} = -(\kappa_\lambda - \sigma_{s,\lambda} F_d) I_\lambda^- + \sigma_{s,\lambda}(1 - F_d) I_\lambda^+ + \kappa_\lambda I_{b,\lambda}(T(y)) \tag{2.7}$$

here F_d is the fraction of radiation scattered in the forward hemisphere, and is derived from the scattering phase function. Adding this term to the equations allows for a more detailed characterization of the scattering process, compared to an isotropic scattering assumption. F_d depends on the optical properties of the medium and its' calculation

will be explained in the relevant section. The boundary conditions for the two equations are:

$$I_\lambda^+(y=0) = G_\lambda \tau_{a\to nf,\lambda} + \alpha_{g,\lambda} I_{b,\lambda}(T(0)) + \rho_{nf\to a,\lambda} I_\lambda^- \tag{2.8}$$

$$I_\lambda^-(y=H) = \rho_{w,\lambda} I_\lambda^+ + \epsilon_{w,\lambda} I_{b,\lambda}(T(H)) \tag{2.9}$$

where G_λ is incident spectral intensity; $\rho_{w,\lambda}$ is wall spectral reflectivity, $\alpha_{g,\lambda}$ is glass spectral absorptivity, $\epsilon_{w,\lambda}$ is wall spectral emissivity and H is the collector depth. $\tau_{a\to nf}$ and $\rho_{nf\to a}$ denote the glass cover's transmissivity from air to the nanofluid, and reflectivity from nanofluid to air. A diagram of the system can be seen in Figure 2.1. $I_{b,\lambda}$ is given by [40]:

$$I_{b,\lambda}(T) = \frac{2hc^2}{\lambda^5} \frac{1}{e^{\frac{hc}{\lambda k_b T}} - 1} \tag{2.10}$$

where h is Planck's constant and k_b is Boltzmann's constant.

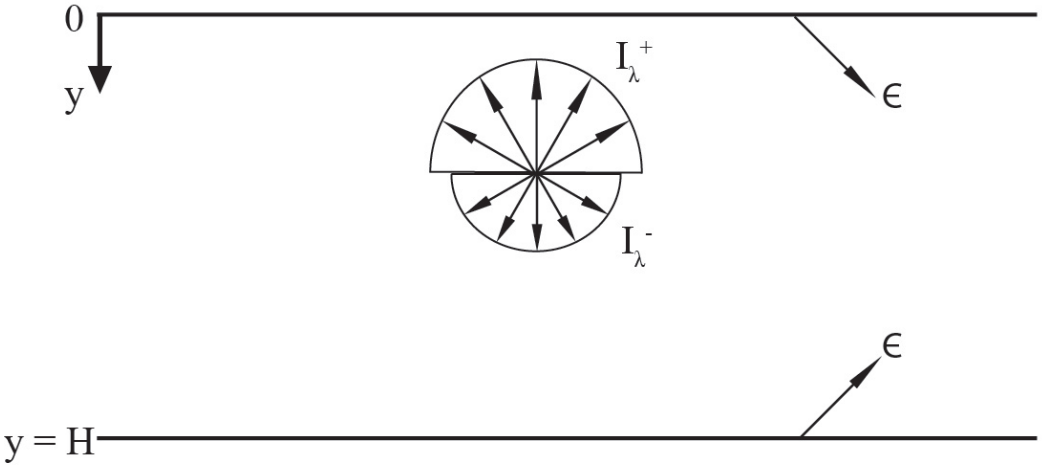

Figure 2.1. Two-Flux approximation diagram.

Transmissivity and reflectivity were obtained using the generalized Fresnel formalism. Transmissivity for the incoming solar radiation was calculated by assuming it to be at normal incidence to the glass cover. The glass complex transmission coefficient

$\tilde{t}_g$ and complex reflection coefficient $\tilde{r}_g$, for a single wavelength, is obtained via [41]:

$$\tilde{r}_g = \frac{\tilde{r}_{a\to g} + \tilde{r}_{g\to nf} e^{-4\pi i \eta_0 d\tilde{n}_g}}{1 + \tilde{r}_{a\to g}\tilde{r}_{g\to nf} e^{-4\pi i \eta_0 d\tilde{n}_g}} \tag{2.11}$$

$$\tilde{t}_g = \frac{\tilde{t}_{a\to g}\tilde{t}_{g\to nf} e^{-2\pi i \eta_0 d\tilde{n}_g}}{1 + \tilde{r}_{a\to g}\tilde{r}_{g\to nf} e^{-4\pi i \eta_0 d\tilde{n}_g}} \tag{2.12}$$

with interface reflection and transmission coefficients defined as:

$$\tilde{r}_{a\to g} = \frac{\tilde{n}_a - \tilde{n}_g}{\tilde{n}_a + \tilde{n}_g} \tag{2.13}$$

$$\tilde{r}_{g\to nf} = \frac{\tilde{n}_g - \tilde{n}_{nf}}{\tilde{n}_g + \tilde{n}_{nf}} \tag{2.14}$$

$$\tilde{t}_{a\to g} = \frac{2\tilde{n}_a}{\tilde{n}_a + \tilde{n}_g} \tag{2.15}$$

$$\tilde{t}_{g\to nf} = \frac{2\tilde{n}_g}{\tilde{n}_g + \tilde{n}_{nf}} \tag{2.16}$$

where $\tilde{n}$ is complex index of refraction, d is the glass thickness, η_0 is wavenumber of radiation in vacuum. The transmissivity from air to nanofluid can then be computed [41]:

$$\tau_{a\to nf} = \left(\frac{n_{nf}}{n_a}\right) \tilde{t}_g \tilde{t}_g^* \tag{2.17}$$

where n is the real part of $\tilde{n}$ and * denotes complex conjugate. For reflectivity from nanofluid to air the radiative flux is assumed to be diffuse and only the interface between the nanofluid and glass is considered. The angular reflection coefficients are computed for orthogonal and parallel polarizations using:

$$\tilde{r}_{nf\to air,\perp} = \frac{\tilde{n}_{nf} cos\theta - \tilde{n}_g cos\chi}{\tilde{n}_{nf} cos\theta + \tilde{n}_g cos\chi} \tag{2.18}$$

$$r_{nf\to air,\parallel} = \frac{\tilde{n}_{nf} cos\chi - \tilde{n}_g cos\theta}{\tilde{n}_{nf} cos\chi + \tilde{n}_g cos\theta} \tag{2.19}$$

where χ, the angle of refraction, is obtained from Snell's law:

$$\chi = sin^{-1}\big(sin\theta \frac{\tilde{n}_{nf}}{\tilde{n}_g}\big) \tag{2.20}$$

Angular spectral reflectivity (as a function of angle of incidence θ) is then:

$$\rho_{nf\to g}(\theta) = \frac{r_{nf\to air,\perp} r^*_{nf\to air,\perp} + r_{nf\to air,\parallel} r^*_{nf\to air,\parallel}}{2} \tag{2.21}$$

Total spectral reflectance is computed by averaging Equation 2.21 over the hemisphere:

$$\rho_{nf\to g} = \int_0^{\pi/2} R_{nf\to g}(\theta) cos\theta sin\theta d\theta \tag{2.22}$$

Solving the Equations 2.6 and 2.7 for I^+_λ and I^-_λ, the spectral intensity is obtained with Equation 2.5. Divergence of the radiative heat flux is obtained with Equation 2.2, and is used as a heat generation profile in the energy balance equation.

2.3. Nanofluid Properties

2.3.1. Radiative Property Modelling of Nanoparticles

Modelling the radiative properties of nanofluids necessitate the estimation of the radiative properties of both their constituent nanoparticles and base fluid. The two main radiative properties of a particle subject to incident radiation are the spectral scattering cross section $C_{s,\lambda}$ and absorption cross section $C_{a,\lambda}$. These two terms are obtained from the solutions of Maxwell's equations, and can be expressed analytically for simple geometries such as spheres. From these, the spectral absorption and scattering efficiencies are calculated via:

$$Q_{a,\lambda} = \frac{4C_{a,\lambda}}{\pi D^2}; \quad Q_{s,\lambda} = \frac{4C_{s,\lambda}}{\pi D^2} \tag{2.23}$$

where D is the particle diameter. Multiplying with the total number of particles inside the medium, the total absorption and scattering efficiencies can be obtained. The number of particles N can be replaced by defining the volume fraction of the

nanofluid:

$$f_v = N\frac{\pi D^3}{6} \tag{2.24}$$

Using Equation 2.24 the spectral absorption and scattering coefficients become:

$$\kappa_\lambda = \frac{3f_v}{2D}Q_{a,\lambda}; \qquad \sigma_{s,\lambda} = \frac{3f_v}{2D}Q_{s,\lambda} \tag{2.25}$$

The optical and radiative properties of a system highly depends on the length scale and scattering characteristics of its constituents' interaction with electromagnetic radiation. The length scale is crucial when considering a model that efficiently and accurately describes the system's properties. An important parameter for defining particle size with respect to incoming radiation is the size parameter ξ:

$$\xi = \frac{\pi D}{\lambda_m} \tag{2.26}$$

here λ_m is the wavelength of incident radiation within the medium. It is also important to determine whether the scattering regime for the system lies in the dependent or independent scattering regime. Dependent scattering regime results in overall lower attenuation of radiative energy due to decreased scattering cross-section. For the case of nanofluids, which are the main focus of this study, the scattering regime stays in the independent range due to low particle loadings and small particles sizes as seen in Figure 2.2.

In the case of particles and agglomerates there are three main methods that correspond to different size parameter intervals. These are Geometric Optics Approximation (GOA) , Rayleigh Scattering Approximation (RSA) and Lorenz-Mie Theory (LMT). The range of validity of these methods with respect to the size parameter can be also be seen in Figure 2.2. These ranges are for spherical particles and were taken from [38].

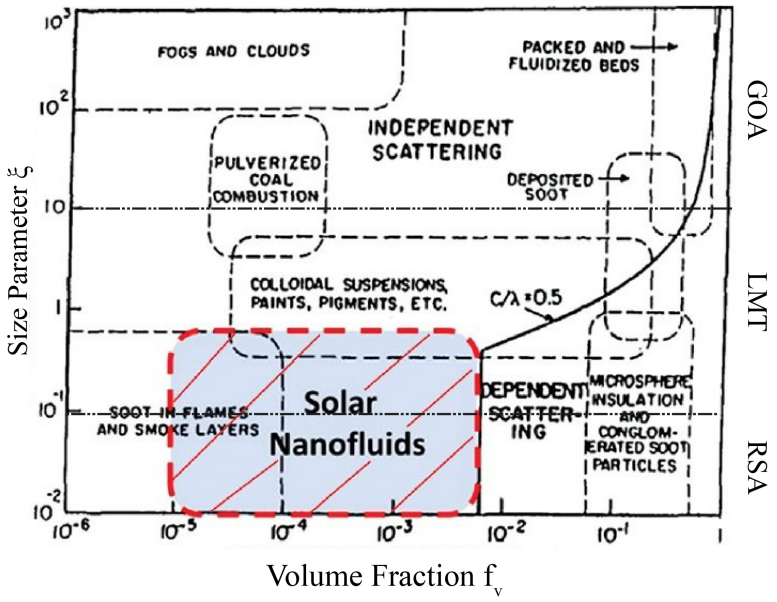

Figure 2.2. Scattering regime map for various dispersed media [42].

Geometric Optics Approximation is suitable for large particles or large size parameters. The main principle is to assume that the incident radiation is composed of rays, whose interaction with the particle depends on the incident angle of the ray hitting the particle and the refractive indices of the particle and surrounding medium. Given these three parameters the change in intensity and polarization for each ray can be calculated by Fresnel equations. The size parameter for nanoparticles is too small for the geometric optics approximation, therefore this method is not suitable for the modelling of nanofluid optical properties.

Another method that can be used to model optical properties is the Rayleigh Scattering Approximation. Rayleigh approximation is valid for particles with size parameters smaller than unity. The scattering cross-section of a particle is proportional to the fourth power of its size parameter:

$$C_{s,\lambda} = \frac{8}{3}\frac{\pi D^2}{4}\xi^4 \left|\frac{m^2-1}{m^2+2}\right|^2 \tag{2.27}$$

where m is the ratio of particle's complex refractive index to medium's complex refractive index

$$m = \frac{n_p - ik_p}{n_m - ik_m} \tag{2.28}$$

here n is the refractive index, k is the extinction coefficient, and subscripts p and m denote particle and medium. From Equation 2.27 it is possible to obtain the scattering efficiency via Equation 2.23:

$$Q_{s,\lambda} = \frac{8}{3}\xi^4 \left|\frac{m^2 - 1}{m^2 + 2}\right|^2 \tag{2.29}$$

The absorption efficiency for RSA also dependes on the fourth power of the size parameter:

$$Q_{a,\lambda} = -4\xi Im\left(\frac{m^2 - 1}{m^2 + 2}\right) \tag{2.30}$$

Rayleigh scattering assumption gives a symmetric phase function with no dependence on the azimuthal angle and with equal forward and backward scattering:

$$\Phi(\theta) = \frac{3}{4}(1 + cos^2\theta) \tag{2.31}$$

2.3.2. Lorenz-Mie Theory

Lorenz-Mie Theory was first formulated as the solution to Maxwell's Equations for a homogeneous and isotropic spherical body within a non-absorbing medium subject to an incident plane-parallel electromagnetic wave. The electric and magnetic fields obtained from this theory can be used to determine the particle's scattering and absorption rates of incident radiation. Because it is a general solution, it can be applied for both small and large particles. Lorenz-Mie Theory is valid for spherical nanoparticles considered in this study. The scattering, extinction and absorption cross-sections

for a single homogeneous sphere is given by [43]:

$$C_{s,\lambda} = \frac{2\pi}{\eta_0^2} \sum_{n=1}^{\infty} (2n+1)(|a_n|^2 + |b_n|^2) \tag{2.32}$$

$$C_{e,\lambda} = \frac{2\pi}{\eta_0^2} \sum_{n=1}^{\infty} (2n+1) Re(a_n + b_n) \tag{2.33}$$

$$C_{a,\lambda} = C_{e,\lambda} - C_{s,\lambda} \tag{2.34}$$

where η_0 is the wave-number of the incident radiation and the coefficients a_n and b_n are (assuming the permeability of the particle and the surrounding medium are equal):

$$a_n = \frac{m\psi_n(mx)\psi_n'(x) - \psi_n(x)\psi_n'(mx)}{m\psi_n(mx)\xi_n'(x) - \xi_n(x)\psi_n'(mx)} \tag{2.35}$$

$$b_n = \frac{m\psi_n(mx)\psi_n'(x) - m\psi_n(x)\psi_n'(mx)}{m\psi_n(mx)\xi_n'(x) - m\xi_n(x)\psi_n'(mx)} \tag{2.36}$$

here ψ_n and ξ_n are Riccati-Bessel functions and $'$ denotes derivative.

Lorenz-Mie Theory is suitable for the modelling of core-shell nanoparticles as well, and it can be extended to include different concentric material shells surrounding a core [44]. For core-shell particles the coefficients a_n and b_n are given as:

$$a_n = \frac{\psi_n(y)\left[\psi_n'(m_2y) - A_n\chi_n'(m_2y)\right] - m_2\psi_n'(y)\left[\psi_n(m_2y) - A_n\chi_n(m_2y)\right]}{\xi_n(y)\left[\psi_n'(m_2y) - A_n\chi_n'(m_2y)\right] - m_2\xi_n'(y)\left[\psi_n(m_2y) - A_n\chi_n(m_2y)\right]} \tag{2.37}$$

$$b_n = \frac{m_2\psi_n(y)\left[\psi_n'(m_2y) - B_n\chi_n'(m_2y)\right] - \psi_n'(y)\left[\psi_n(m_2y) - B_n\chi_n(m_2y)\right]}{m_2\xi_n(y)\left[\psi_n'(m_2y) - B_n\chi_n'(m_2y)\right] - \xi_n'(y)\left[\psi_n(m_2y) - B_n\chi_n(m_2y)\right]} \tag{2.38}$$

$$\tag{2.39}$$

here ψ_n and χ_n are Riccati-Bessel functions, and subscripts 1 and 2 denote core and shell relative refractive index. The coefficients A_n and B_n are:

$$A_n = \frac{m_2\psi_n(m_2x)\psi_n'(m_1x) - m_1\psi_n'(m_2x)\psi_n(m_1x)}{m_2\chi_n(m_2x)\psi_n'(m_1x) - m_1\chi_n'(m_2x)\psi_n(m_1x} \tag{2.40}$$

$$B_n = \frac{m_2\psi_n(m_1x)\psi_n'(m_2x) - m_1\psi_n(m_2x)\psi_n'(m_1x)}{m_2\chi_n'(m_2x)\psi_n(m_1x) - m_1\chi_n(m_2x)\psi_n'(m_1x} \tag{2.41}$$

Phase functions can be approximated using the wavelength dependent asymmetry factor g calculated using:

$$g = \frac{1}{Q_{s,\lambda}} \frac{4}{\xi^2} \left\{ \sum_{n=1}^{\infty} \frac{n(n+2)}{n+1} Re(a_n a_{n+1}^* + b_n b_{n+1}^*) + \sum_{n=1}^{\infty} \frac{2n+1}{n(n+1)} Re(a_n b_n^*) \right\} \tag{2.42}$$

This dimensionless parameter ranges from -1 for fully backward scattering to 1 for fully forward scattering and it takes the value 0 for isotropic scattering. The phase function used in this study was proposed by Henyey and Greenstein [45] and serves as a good approximation for the LMT result [38]:

$$\Phi_{HG}(\mu) = \frac{(1-g^2)}{(1+g^2-2g\mu)^{\frac{3}{2}}} \tag{2.43}$$

where μ is the cosine of the scattering angle θ. This phase function also assumes azimuthal symmetry of the scatterer with respect to the incident radiation, hence it does not depend on ϕ. From Equation 2.43 it is possible to find the forward to backward scattering ratio F_d, to be used in the radiation model:

$$F_d = \frac{\int_0^1 \Phi_{HG} d\mu}{\int_{-1}^1 \Phi_{HG} d\mu} \tag{2.44}$$

2.3.3. Size Dependence of the Optical Properties of Nanoparticles

The dielectric function of bulk materials can be modelled classically using the Drude Model based on the oscillatory reaction of electrons to the electric field component of incoming electromagnetic waves [44]

$$\epsilon(\omega) = 1 - \frac{\omega_p}{\omega^2 + i\omega\gamma} \tag{2.45}$$

where ω is the circular frequency; ω_p and γ are the plasma frequency and free electron relaxation frequency of the material. This model corresponds to the reaction of free electrons to electromagnetic radiation of frequency ω. Certain materials also show

interband transitions, that is transitions of the electron from a bound state to the conduction band. For most metals, the energy gap for this process is large enough that the Drude Model is sufficient. The optical response of the bound electrons must be accounted for materials that do show interband transitions, such as noble metals. To incorporate these transitions, additional terms for each oscillator mode must be added. This extended model is called the Drude-Lorentz Model [44]:

$$\epsilon(\omega) = 1 - \frac{\omega_p}{\omega^2 + i\omega\gamma} + \sum_j \frac{\omega_{p,j}}{\omega_{bound,j} - \omega^2 - i\omega\gamma_{bound,j}} \tag{2.46}$$

here $\omega_{bound,j}$ is the resonance frequency for the jth oscillator. For the case of gold, silver and copper; it is sufficient to consider the contribution of the single electron in the valence band which gives:

$$\epsilon(\omega) = 1 - \frac{\omega_p}{\omega^2 + i\omega\gamma} + \frac{\omega_p}{\omega_{bound} - \omega^2 - i\omega\gamma_{bound}} \tag{2.47}$$

Measurements of the bulk dielectric function can also be fitted to a Drude-Lorentz Model:

$$\epsilon_{bulk}(\omega) = 1 - \frac{\omega_p}{\omega^2 + i\omega\gamma_{bulk}} + \frac{\omega_p}{\omega_{bound} - \omega^2 - i\omega\gamma_{bound,bulk}} \tag{2.48}$$

Subtracting Equation 2.48 from Equation 2.47, it is possible to eliminate the bound part of the dielectric function. This gives:

$$\epsilon(\omega) = \epsilon_{bulk}(\omega) + \frac{\omega_p}{\omega^2 + i\omega\gamma_{bulk}} - \frac{\omega_p}{\omega^2 + i\omega\gamma} \tag{2.49}$$

For particles sizes smaller than the bulk mean free path of the electrons, Equation 2.49 must be modified. This is achieved by modifying the relaxation coefficient γ using

the following relation [46]:

$$\gamma = \gamma_{bulk} + A\frac{v_f}{l_{eff}} \tag{2.50}$$

where v_f is the Fermi velocity of the metal, l_{eff} is the effective mean free path of the electron, and A is a fitting parameter. The effective mean free path of the electron depends mainly on the geometry of the particle and the scattering properties of the electrons at the particle's surface [44]. For a sphere, scattering can either be diffusive or isotropic. The effective mean free path for the two cases are [46]:

$$l_{eff,diffusive} = r \tag{2.51}$$

$$l_{eff,isotropic} = \frac{4r}{3} \tag{2.52}$$

where r is the radius of the particle.

There have been various proposals for the effective mean free path for the shell region of a core-shell particle [47], [48]. Moroz [49] derived the mean free path using billiard scattering model:

$$l_{eff,billiard} = \frac{4(r_{shell}^3 - r_{core}^3)}{3(r_{shell}^2 + r_{core}^2)} \tag{2.53}$$

The advantage of Equation 2.53 is that it recovers the linear dependence on r in the thin-shell limit. In this study isotropic scattering is assumed for pure nanoparticles (Equation 2.52). For core-shell nanoparticles Equation 2.53 is employed. The parameter A in Equation 2.50 is an empirical constant on the order of 1. Different values of A has been reported in the literature ranging from 0.7 to 3 [44], and no single value is universally accepted. In light of this, we have chosen $A = 1$ as recommended in [36]. Bulk values of γ, v_f, ω_p were taken from [50]. Bulk complex dielectric function was calculated using experimental complex index of refraction data from [51] and the

relations:

$$\epsilon_1 = n^2 - k^2 \tag{2.54}$$

$$\epsilon_2 = 2nk \tag{2.55}$$

where ϵ_1 and ϵ_2 are the real and imaginary parts of the complex dielectric function and n and k are the real and imaginary parts of the complex index of refraction.

2.3.4. Radiative Properties of Nanofluids

To characterize the absorption properties of nanofluids, their radiative properties must be calculated. Spherical nanoparticles, core-shell or single material, can be accurately modelled using Lorenz-Mie Theory (LMT), which is also suitable for the characterization of scattering properties of larger nanoparticles. The optical properties of nanoparticles were calculated using the LMT implementation of Mätzler [52].

Nanofluids with particle volume concentration less than 0.6% lie in independent scattering regime [41]. Nanofluids considered here have volume fractions that are usually below this limit, therefore independent scattering is assumed. The absorption and scattering coefficients of nanoparticles were calculated using Equation 2.25. The extinction coefficient for the nanoparticle was obtained using:

$$\beta_{\lambda,np} = \kappa_{\lambda,np} + \sigma_{s,\lambda,np} \tag{2.56}$$

Scattering at the wavelength range important for solar radiation is negligible for base fluids and their extinction coefficients can be calculated directly from the imaginary part of their complex dielectric function:

$$\kappa_{\lambda,bf} = \beta_{\lambda,bf} = \frac{4\pi k_{bf}}{\lambda} \tag{2.57}$$

where bf denotes base fluid and k is the imaginary part of the complex refractive index at wavelength λ. The contribution of the nanoparticle and base fluid optical properties are linear [53]. Thus, it is possible to find the total extinction coefficient of the nanofluid by simply adding them:

$$\beta_{\lambda,nf} = \beta_{\lambda,np} + \beta_{\lambda,bf} \tag{2.58}$$

This linearity also holds for absorption and scattering coefficients of the nanofluid.

2.3.5. Thermo-pyhsical properties

The specific heat capacity of the nanofluids were calculated using classical mixture theory [54]. For core-shell nanofluids, effective specific heat capacity were first calculated for the core-shell nanoparticle and then for the nanofluid. The expressions used are:

$$c_{p,eff} = \frac{f_v(\rho_1 c_{p,1}) + (1 - f_v)(\rho_2 c_{p,2})}{f_v\rho_1 + (1 - f_v)\rho_2} \tag{2.59}$$

where c_p, ρ, f_v are specific heat capacity, density and volume fraction and subscript eff denotes effective value and 1 and 2 denotes media. For nanoparticles subscript 1 represents core and 2 represents shell material, whereas for the nanofluid 1 represents the core-shell or pure nanoparticle and 2 the base fluid. Density of core-shell nanoparticles and nanofluids were also obtained with the mixture method:

$$\rho_{eff} = f_v\rho_1 + (1 - f_v)\rho_2 \tag{2.60}$$

For the thermal conductivity of the core-shell nanofluid the following correlation, valid at low volume fractions, is used [55]:

$$k_{nf} = k_{bf}\left[\frac{2(1 - f_v) + (1 + 2f_v)(B/A)}{(2 + f_v) + (1 - f_v)(B/A)}\right] \tag{2.61}$$

here k_{nf}, and k_{bf} are the thermal conductivity of the nanofluid and base fluid respectively. Constants A and B are defined as:

$$A = 1 + 2\delta^3 - (1 - \delta^3)\frac{k_{core}}{k_{shell}} \tag{2.62}$$

$$B = (2 + \delta^3)\frac{k_{core}}{k_{bf}} - 2(1 - \delta^3)\frac{k_{shell}}{k_{bf}} \tag{2.63}$$

where δ is the ratio of the shell radius to core radius. For pure nanoparticles this expression reduces to the Maxwell-Garnett effective medium model of thermal conductivity:

$$\frac{k_{nf}}{k_{bf}} = \frac{k_{np} + 2k_{bf} + 2f_v\,(k_{np} - k_{bf})}{k_{np} + 2k_{bf} - f_v\,(k_{np} - k_{bf})} \tag{2.64}$$

These models are considered valid for the volume fraction range practical for solar nanofluids since thermal conductivity enhancement of nanofluids, with both metal and carbon-based nanoparticles, are not significant at these particle loadings [56]. The viscosity of the nanofluid is modelled according to Brinkman's viscosity model which holds for volume fraction values of up to 4% [57]:

$$\mu_{nf} = (1 - f_v)^{-2.5}\mu_{bf} \tag{2.65}$$

where μ_{nf} and μ_{bf} are the dynamic viscosities of the nanofluid and the base fluid respectively.

2.4. Convection Model

Flow and heat transfer models for nanofluids can be classified as single-phase or two-phase [58]. Two-phase flow method models the base fluid and particles as separate continua. Depending on how the continuity, momentum and energy equations of the fluid and particles are evaluated, three methods are applicable [59]:

(i) The Volume of Fluid method, which solves the flow and energy equations as a mixture phase and the continuity equation separately for the two phases.

(ii) Mixture Model, which can be used when velocities of the phases are not the same. This method solves momentum, continuity and energy equations for the mixture, volume fraction equation for the particle and then uses correlations to find the velocities of the two phases.

(iii) Eulerian Model, which solves separate continuity, momentum and energy equations for both phases. Interactions between phases are tracked to account for heat and momentum transfer between phases.

Single phase flow models assume the fluid to be a single continuum. Both phases are assumed to have the same temperature and velocity field [60]. This requires the calculation of effective properties for the nanofluid through the use of a specified volume fraction of the second phase. These effective parameters may also depend on particle size and shape [61].

Göktepe *et al.* [62] investigated the performance and accuracy of single and two phase models and showed that while two phase flows are more accurate, they overestimate heat transfer characteristics and are significantly more computationally expensive. Single phase models on the other hand underestimate the results and while slightly less accurate, they still show reasonable agreement with experiments. Because of this, and the fact that it is not resource intensive, single phase flow model is chosen in this work along with the following simplifications to the energy Equation 2.3: Two-Dimensional System, Steady-State\Time Independent, Constant Flow Profile, Incompressible Flow.

With these assumptions the energy equation becomes:

$$\rho c_p U(y) \frac{\partial T}{\partial x} = k \frac{\partial^2 T}{\partial y} - \frac{\partial q_r}{\partial y} \tag{2.66}$$

where T is the temperature, ρ, c_p and k are the density, specific heat capacity and thermal conductivity of the nanofluid, $U(y)$ is the flow profile and q_r is the radiative heat flux. The flow boundary conditions are no-slip at interfaces. The flow profile for

the flat plate collector is approximated as fully developed laminar flow between parallel plates:

$$v(y) = 6U_{mean}\left[\frac{y}{H} - \left(\frac{y}{H}\right)^2\right] \tag{2.67}$$

here H is receiver depth and U_{mean} is the mean flow velocity.

Boundary conditions for Equation 2.66 are:

$$-k_c \left.\frac{\partial T}{\partial y}\right|_{y=0} = h_{conv}(T_{amb} - T(0)) \tag{2.68}$$

$$0 = -k_c \left.\frac{\partial T}{\partial y}\right|_{y=H} + q_r(H) \tag{2.69}$$

$$T(x=0) = T_{in} \tag{2.70}$$

h_{conv} is the combined top loss coefficient and T_{in} is the inlet temperature. The top boundary condition is convective loss to the ambient and bottom boundary condition is adiabatic wall. Schematic of the system can be seen in Figure 2.3.

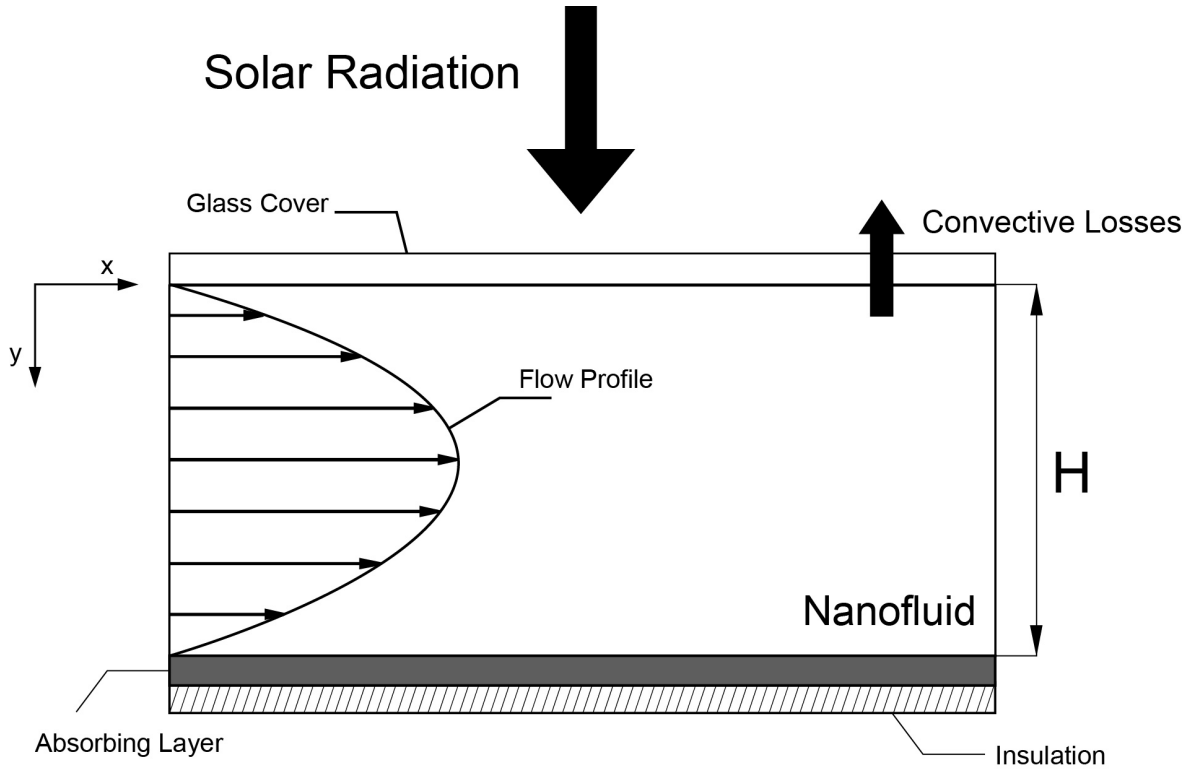

Figure 2.3. Schematic of the flat plate Model.

3. PROBLEM STATEMENT AND FORMULATION

3.1. Geometry and Physical Model

The solar radiation was approximated as blackbody emission with the temperature of the sun assumed to be $T_{sun} = 5800K$. Geometry and parameters for the flat plate and parabolic collector cases are described below.

3.1.1. Flat Plate Collector

The flat plate collector was modelled as a two-dimensional system with a glass cover at the top and and insulation at the bottom. Convective heat loss is assumed to occur only from the top of the system. Flow profile is assumed laminar, fully developed. Outside convective heat loss coefficient was chosen to be $h_{conv} = 6.43$ W/m^2, following experimental results reported in [63]. Receiver depth thickness, collector length were set to 1.5 cm and 1.2 m and discretized into 600 and 500 nodes respectively. Wavelength domain ranged from 0.31 μm to 9.9 μm and was divided into 700 increments. Mean velocity was chosen to be 1 mm/s and inlet and ambient temperatures were 30°C and 15°C respectively.

Different nanoparticle, base fluid and volume fractions were investigated in this study. Nanoparticles (NPs) comprised of pure and core-shell gold, silver, copper and aluminium ones. The core material of core-shell NPs was silica. Graphite NPs were also studied and compared with the aforementioned metallic NPs. Nanoparticle radii ranged from 5 nm to 50 nm with 5 nm increments. Two cases for the shell thickness of core-shell NPs were considered: 3 nm and 5 nm. Core-shell NPs with 5 nm shell thickness had radii ranging from 10 nm to 50 nm, whereas 3 nm ones had the same values as the pure NPs. Base fluids considered for water and ethylene glycol and five different volume fraction values were used: 0.05%, 0.01%, 0.005%, 0.001% and 0.0005%. Bottom plate was assumed adiabatic with an absorptivity of 0.89, that is typical for solar absorbers used in conventional flat plate collectors [64].

3.2. Solution Procedure

Since the radiation and energy equations are coupled, they must be solved iteratively. Both the Two-Flux method formulation of RTE and the energy equation were discretized with Cartesian grids with equal spacing and solved using implicit Finite Difference Method. Solution Procedure for the coupled system is as follows:

(i) Calculate radiative and thermo-physical properties of the nanofluid.
(ii) Calculate initial radiative heat flux and divergence of radiative heat flux profile using T_{in}.
(iii) Using these two profiles calculate the temperature profile for the next iteration.
(iv) Using this new temperature profile update thermo-physical properties and obtain the new radiative heat flux and divergence of radiative heat flux.
(v) Continue with the next iteration.

Bulk refractive index for data nanoparticles were obtained from [65] with the exception of graphite, which was taken from [66]. Optical constants of water and ethylene glycol were obtained form [67] and [68], respectively. Refractive index data for the glass cover were taken from [69]. Thermo-physical properties were obtained from [51].

3.3. Performance Metric

To be able to compare nanofluid performance, efficiency terms for the system were defined. Total Efficiency for the collector was found using:

$$\eta_{tot} = \frac{Q_{net}}{CG_iL} \tag{3.1}$$

where C is the concentration ratio of the incident sunlight, L is the length of the receiver, G_i is the incident solar flux calculated with:

$$G_i = \int_0^\infty S_{att}\Omega_s I_{b,\lambda}(T_{sun})d\lambda \tag{3.2}$$

here $S_{att} = 0.73$ is the attenuation coefficient of solar radiation in the atmosphere and $\Omega_s = 6.87 \times 10^{-5}$ is the solid angle subtended by earth with respect to the sun [70]. Q_{net} is the total energy gain of the fluid and is calculated with:

$$Q_{net} = \rho c_p U_{mean}(T_{mean,out} - T_{mean,in}) \tag{3.3}$$

Quantifying the radiation characteristic of the nanofluid required another efficiency term called absorption efficiency:

$$\eta_{abs} = \frac{\int_0^L q_r(y=0)}{\tau_{a\to nf} C G_i L} \tag{3.4}$$

This term describes the ratio of total radiative energy transferred to the nanofluid to the total incident solar radiation, excluding the losses due to transmission through the glass cover. One last efficiency term was defined, called flow efficiency, which quantifies the ratio of net heat gain to that total radiative heat absorbed by the nanofluid:

$$\eta_{flow} = \frac{Q_{net}}{\int_0^L q_r(y=0)} \tag{3.5}$$

total efficiency can be expressed using these two efficiency terms and the transmissivity of the glass cover $\tau_{a\to nf}$:

$$\eta_{tot} = \tau_{a\to nf}\eta_{abs}\eta_{flow} \tag{3.6}$$

4. RESULTS AND DISCUSSION

4.1. Verification Studies

4.1.1. Verification of the Optical Property Model

Verification studies for the optical property model involved verification of the Lorenz-Mie code for core-shell nanoparticles and verification of the size dependence effects.

4.1.1.1. Verification of the Lorenz-Mie code. In order to verify Lorenz-Mie code used in this study, extinction efficiencies for core-shell nanoparticles with silica core and silver shell in water were calculated and compared with numerical results of Quinten [44]. Shell thickness was taken to be 5 nm for all nanoparticles and four different total radius values were used. The results are presented in Figure 4.1 and show excellent agreement with the literature. Both the cited results, and the results of the verification study do not include size dependence effects, whose verification is shown in the next section.

4.1.1.2. Verification of Size Dependence of Optical Properties. Verification of size dependence effects were done using numerical results of Blaber *et al.* [35]. Results are for a gold shell with vacuum core with 37.5 nm core radius and 42.2 nm total radius. The dielectric function was calculated using Equation 2.49 and the gold data from the paper: $\omega_p = 8.55eV$, $\gamma_{bulk} = 0.0184eV$ and $v_f = 1.40 \times 10^6 m/s$. The fitting parameter A was taken to be unity and Equation 2.53 was used to find the mean free path for the shell. The modified dielectric function was used to obtain via Equations 2.54 and 2.55 the modified optical properties. Finally using the LMT code the absorption efficiency of the nanoparticle was obtained. Results showed good agreement.

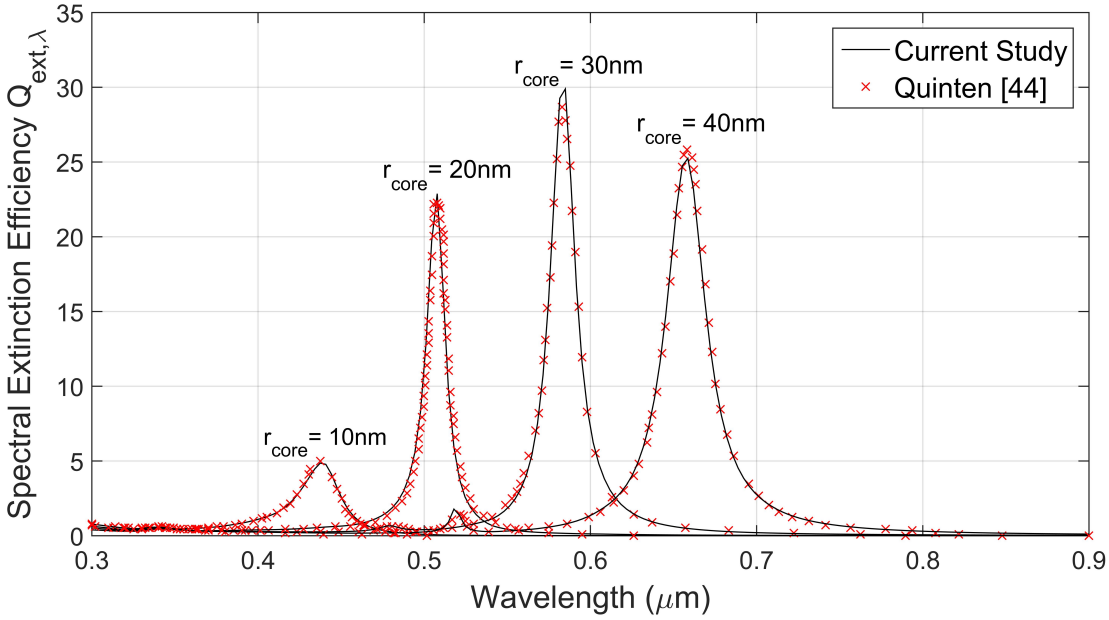

Figure 4.1. Verification results for silica core silver shell nanoparticles with shell thickness 5 nm.

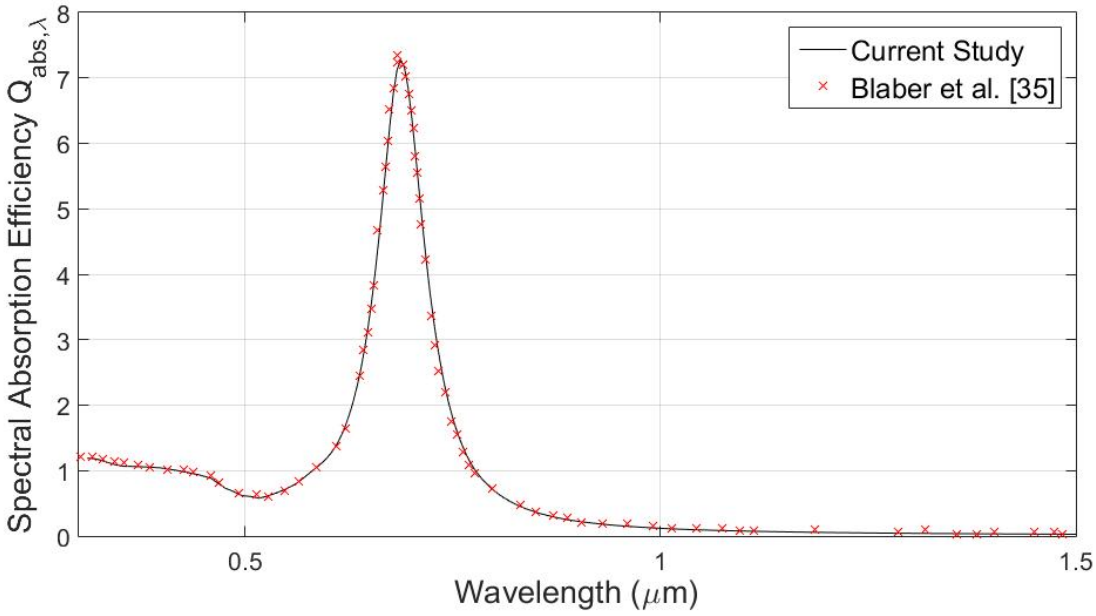

Figure 4.2. Verification results for size dependence of a vacuum core gold shell nanoparticle.

4.1.2. Verification of the Radiation Model

Two-Flux Model was verified using results from Modest [41] for a one-dimensional plane-parallel system with a gray isotropically scattering medium surrounded by two black plates, both at the same temperature. The thermal emission of the medium was also taken into account. Cases considered were $\omega = 0$ (no scattering) and $\omega = 0.5$. Modest presents exact solutions for both cases and also the Two-Flux approximation solution for the case with no scattering. Comparison with the numerical results are shown in Figure 4.3, where the non-dimensional radiative heat flux is plotted against optical thickness of the medium which is defined as:

$$\tau_d = \beta H \tag{4.1}$$

These plots were generated by calculating the radiative flux for different optical thickness values. Verification results for the first case shows very good agreement with the Two-Flux solution of Modest. The slight discrepancy between the two results can be attributed to the fact that the Two-Flux solution was derived analytically for this simple case. For $\omega = 0.5$, the Two-Flux approximation result of this study shows good agreement with the exact solution supplied.

4.1.3. Verification of the Convection Model

The convection model was verified for a case of laminar parallel plate flow with upper and lower plates at the same temperature. Thermal radiation was neglected for this verification study. This case has an analytic solution and the Nusselt number, $Nu = 7.54$, for thermally fully developed flow [71]. Verification conditions were: water with inlet temperature of 23°C, plate temperature of 43°C, plate separation of 5 cm and mean flow velocity of 4.3 mm/s. Results are presented in Figure 4.4. The calculated Nusselt number reaches the expected value and the convection model used in this study is deemed accurate.

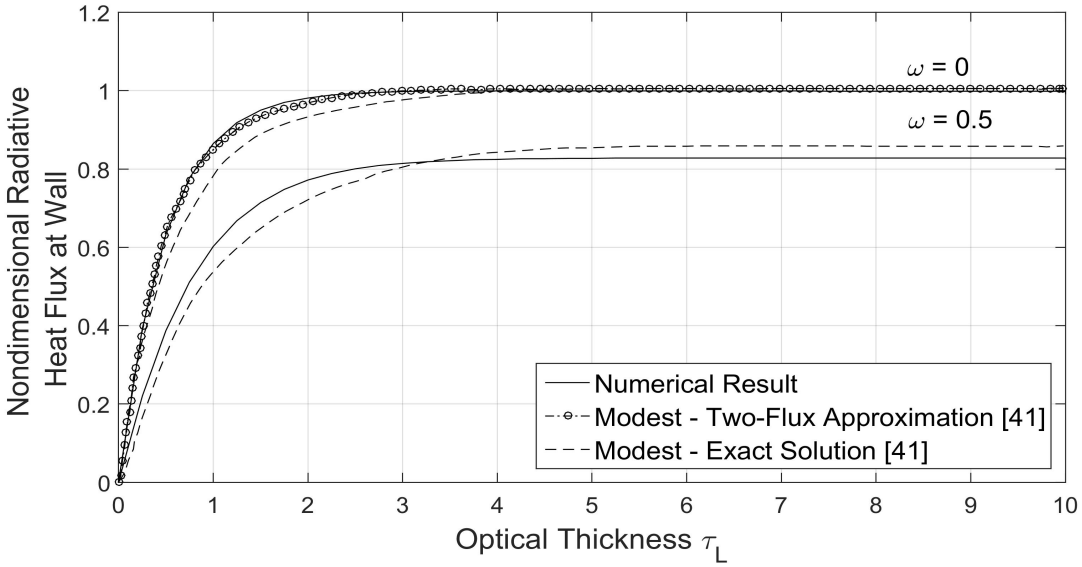

Figure 4.3. Two-Flux model verification.

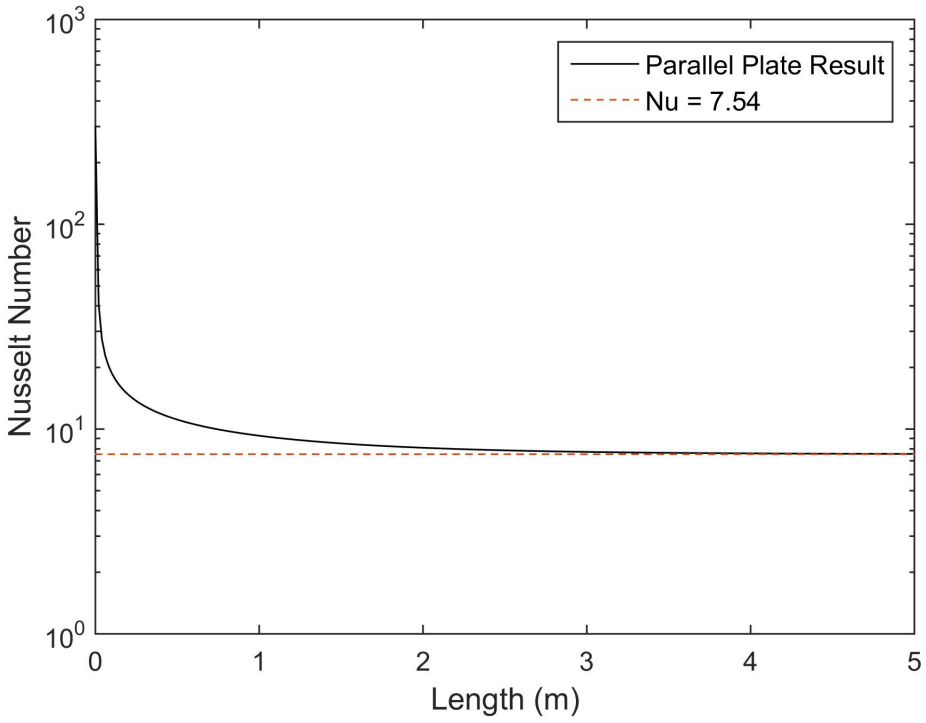

Figure 4.4. Convection model verification.

4.1.4. Verification of the Combined Radiation and Convection Model

The energy equation solution considering convection and radiation was also verified using results reported by Chawla and Chan [72]. The authors studied a laminar flow of an isotropically scattering, incompressible and constant property fluid between two infinitely long parallel plates with a separation of $\tau_d = \beta H$. Schematic of the system is depicted in Figure 4.5. The non-dimensional axial length ζ and non-dimensional height ν are defined as:

$$\zeta = \frac{k\beta^2 x}{\rho c_p U_{mean}} \tag{4.2}$$

$$\nu = \beta y \tag{4.3}$$

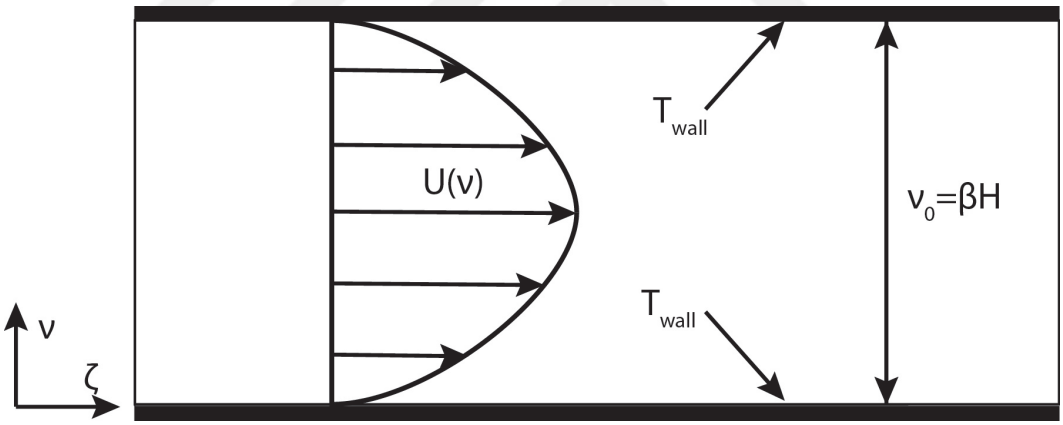

Figure 4.5. Diagram for the combined radiation convection verification study.

The plates were taken to be diffuse and opaque. Radiative properties of both the fluid and the plates were assumed gray. The authors used spline collocation method to solve both the radiative transport equation and energy equation [72]. Results were compared by using the convective and radiative Nusselt numbers defined as follows:

$$Nu_c = \frac{2H}{T_{wall} - T_b}\left(- \left.\frac{\partial T}{\partial y}\right|_{wall}\right) = \frac{2H q_{c,wall}}{k(T_{wall} - T_b)} \tag{4.4}$$

$$Nu_r = \frac{q_{r,wall} H}{k(T_{wall} - T_b)} \tag{4.5}$$

where T_b is the bulk temperature of the fluid given by:

$$T_b = \frac{\int_0^H U(y)T(y)dy}{\int_0^H U(y)dy} \tag{4.6}$$

Total Nusselt number Nu is given by the sum of convective and radiative Nusselt numbers. The two cases considered were: non-scattering medium ($\omega = 0$), plate emissivity ϵ equal to 1; and $\omega = 0.65$ and $\epsilon = 0.5$.

Comparison of calculated Nusselt numbers with the cited results are shown in Figure 4.6 and 4.7.

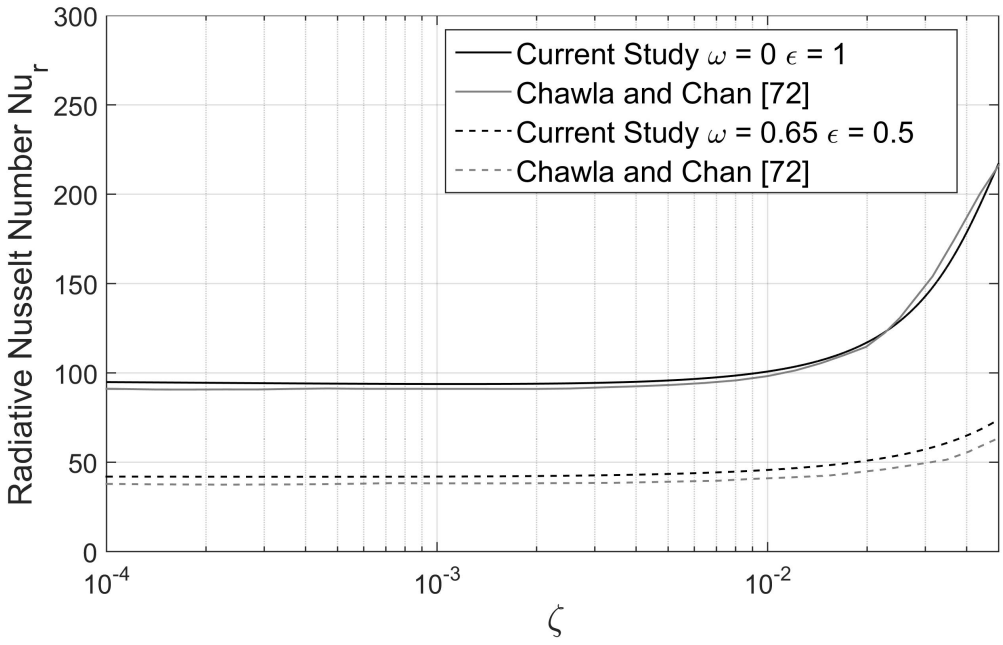

Figure 4.6. Radiative Nusselt number compared with results from literature.

The small deviations at the endpoints with respect to the cited results are mainly due to the Two-Flux approximation used, which is less accurate than the method employed by the authors, namely numerical solution of the RTE in its integral form. The Two-Flux model instead assumes isotropic intensities for forward and backward hemispheres which leads to these deviations. Maximum errors for both Nusselt numbers

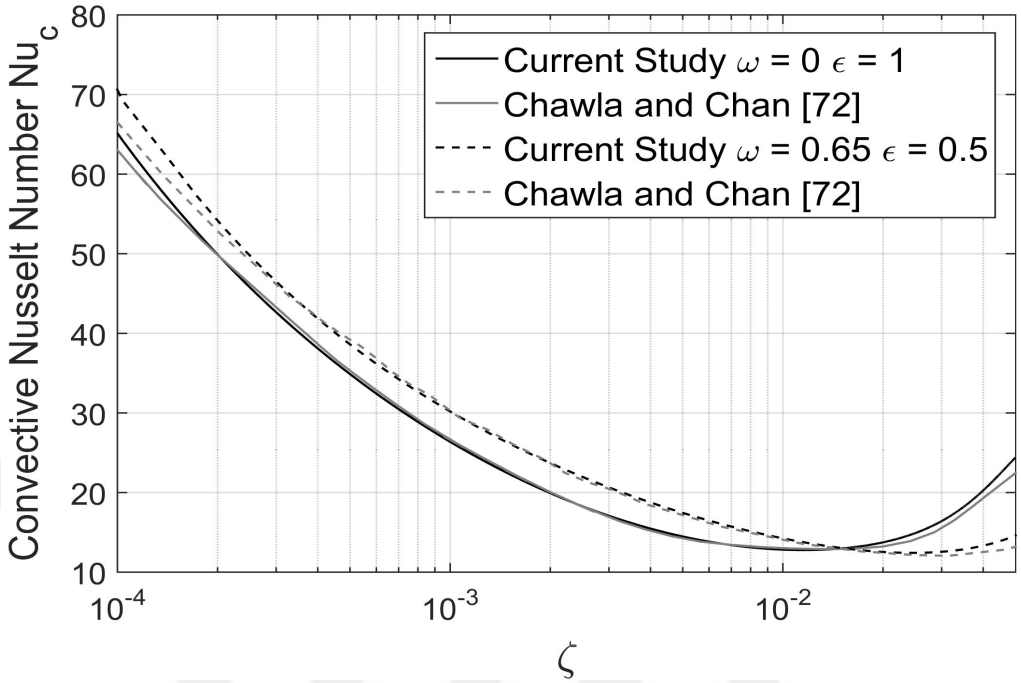

Figure 4.7. Convective Nusselt number compared with results from literature.

were below 5%, and the combined radiation-convection model was deemed acceptable. The convergence behavior of the solution is shown in Figure 4.8. Relative error is defined as:

$$\epsilon_{rel} = |\frac{T^{p+1} - T^{p}}{T^{p+1}}| \tag{4.7}$$

where p denotes iteration number. The good agreement with the literature indicates that the convergence criteria of $\epsilon_{rel} = 10^{-5}$ maximum relative error in temperature is sufficient. The ratio between radiative and conductive heat transfer modes can be quantified with the conduction-radiation parameter N defined as:

$$N = \frac{k\beta}{4\sigma T_{wall}^{3}} \tag{4.8}$$

The case studied has $N = 0.01$ which indicates a radiation dominant system, and convergence is achieved with few iterations. The flat-plate collector model is also

similarly radiation dominant and the same convergence criteria is applied.

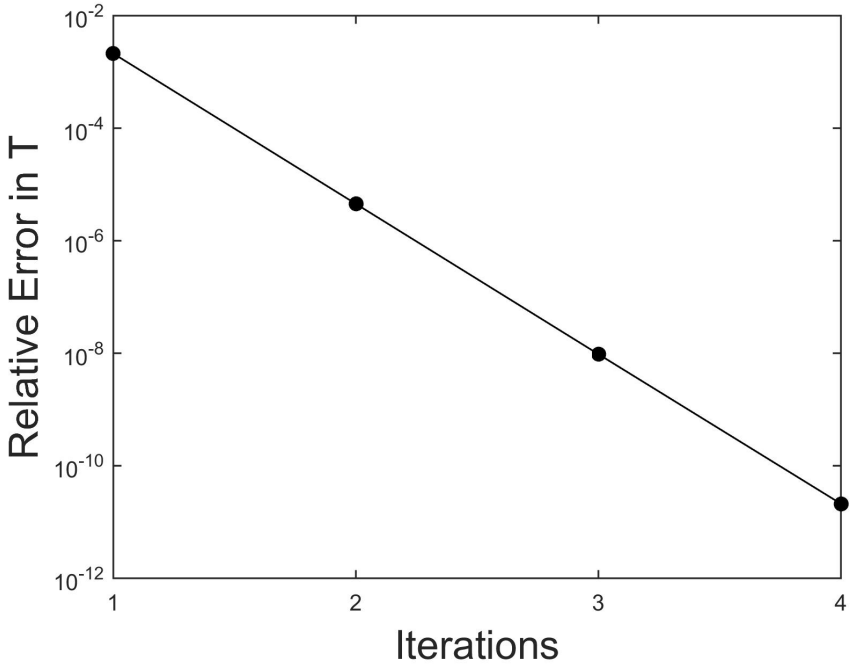

Figure 4.8. Convergence study results.

4.2. Validation Study of the Convection Model

Validation of the Convection model was done using data from experimental tests conducted by Streed et al. [73]. These tests used conventional flat plate collectors with absorbing covers used to capture incident radiation; therefore, the convection model was modified to include an absorbing layer at the top. Since the temperature change of both the fluid and the absorbing layer were not dramatic, convective heat transfer of the fluid was taken to be constant. Results are shown in Figure 4.9. The slight increase in efficiency results can be attributed to the chosen model that neglects heat loss from the bottom. Overall the model reproduced the trend of decreasing efficiency with increasing difference between inlet and ambient temperatures. Maximum difference with experimental efficiency values were less than 5%, and the numerical model was deemed sufficient for the purposes of this study.

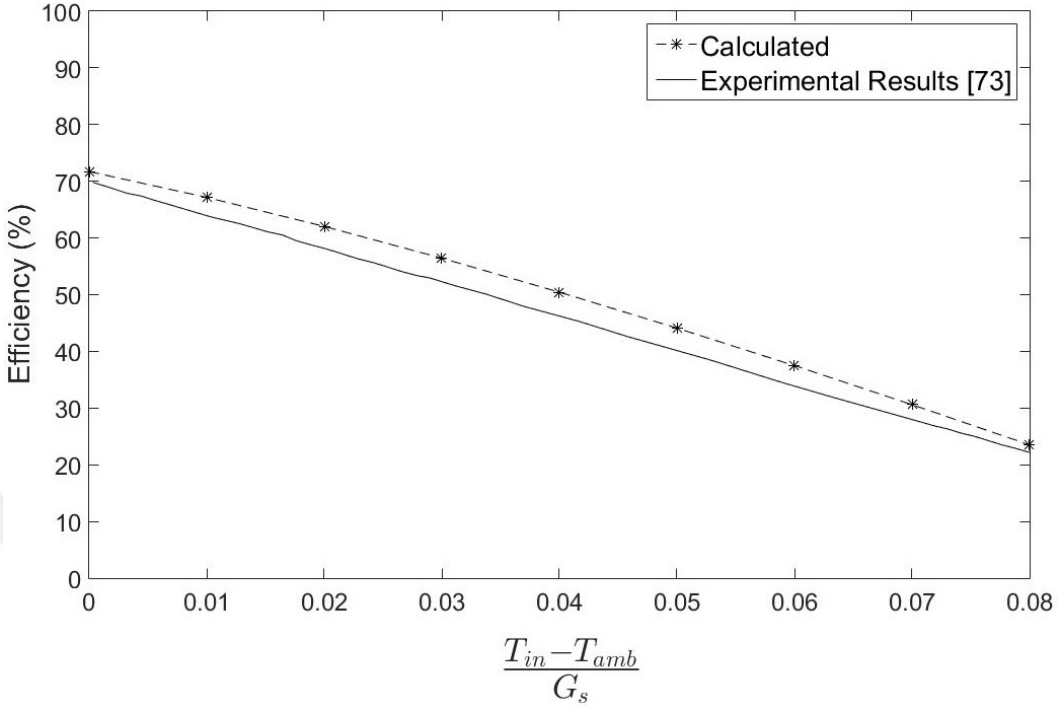

Figure 4.9. Results of the validation study.

4.3. Grid Independence Study

A grid independence study was conducted the flat-plate model. The ΔT profiles at the collector exit were compared for four different x and y node number combinations. Results are displayed in Figure 4.10. Grid independence was achieved using 600 by 500 nodes for y and x respectively. Increasing the number of nodes did not make any significant difference on the temperature profile.

4.4. Radiative Properties of Nanofluids

Radiative properties of nanofluids are highly dependent on particle size, material and volume fraction. A comparison of silver nanofluids with 0.005% volume fraction and water as base fluid with different particle radii is presented in Figure 4.11. The increase in size redshifts and broadens the plasmonic peak, leading to higher extinction in the infrared. The peak value of the extinction coefficient also varies with size, with a maximum observed for a particle radius of 15 nm. The nanoparticle contribution to

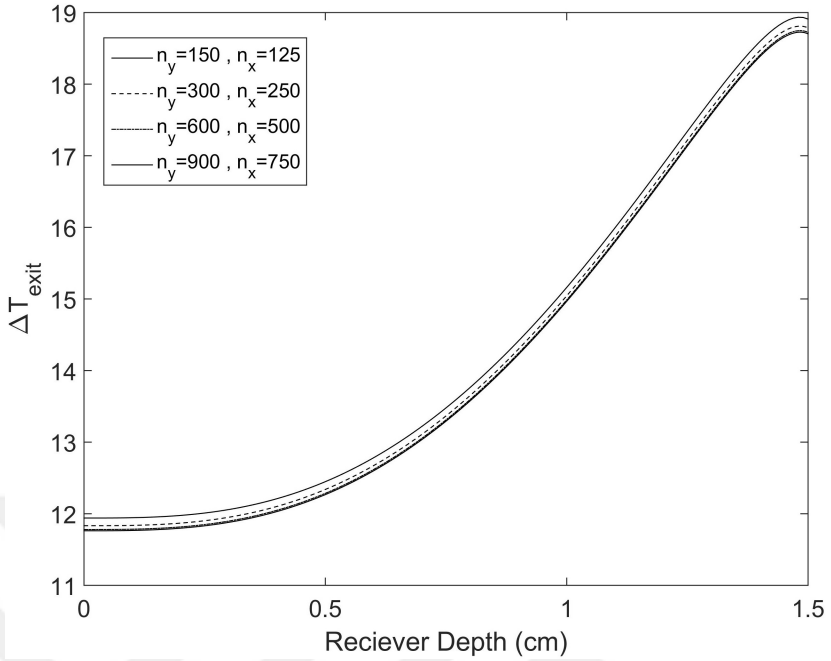

Figure 4.10. Grid independence study.

extinction is minimal after 1.2 μm, which is why all curves merge into a single line that corresponds to the base fluid extinction coefficient.

4.4.1. Effect of the size dependence of dielectric functions

Size dependence of the dielectric function exhibited appreciable impact on the radiative properties of nanoparticles investigated. Figure 4.12 depicts the extinction efficiencies of three gold-water nanofluids with various nanoparticle sizes and volume fraction 0.005%. It is possible to see that as particle size decreases, so does the extinction efficiency value of the corresponding plasmonic peak, and this effect gets more pronounced at smaller particle sizes. At a radius of 20 nm, the change in extinction efficiency is much smaller, due to the total particle size being close that of the the bulk electron mean free path of gold (42 nm). Another consequence of size dependence is the increase of the extinction value at longer wavelengths, and this effect gets more pronounced as particle size decreases.

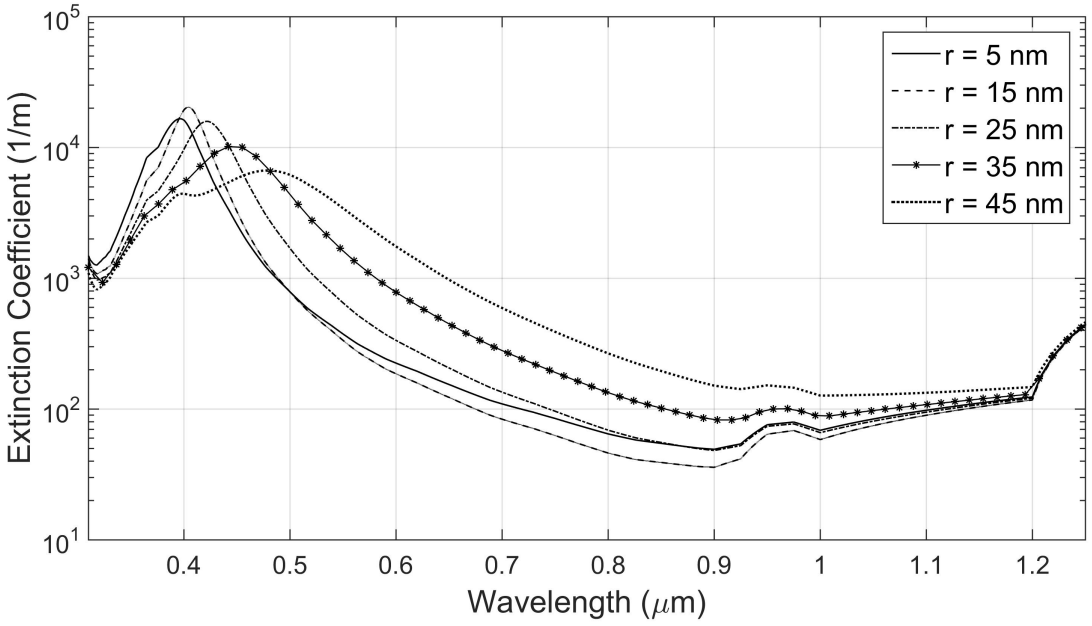

Figure 4.11. Extinction coefficients for silver-water nanofluids with 0.005% volume fraction and different radii.

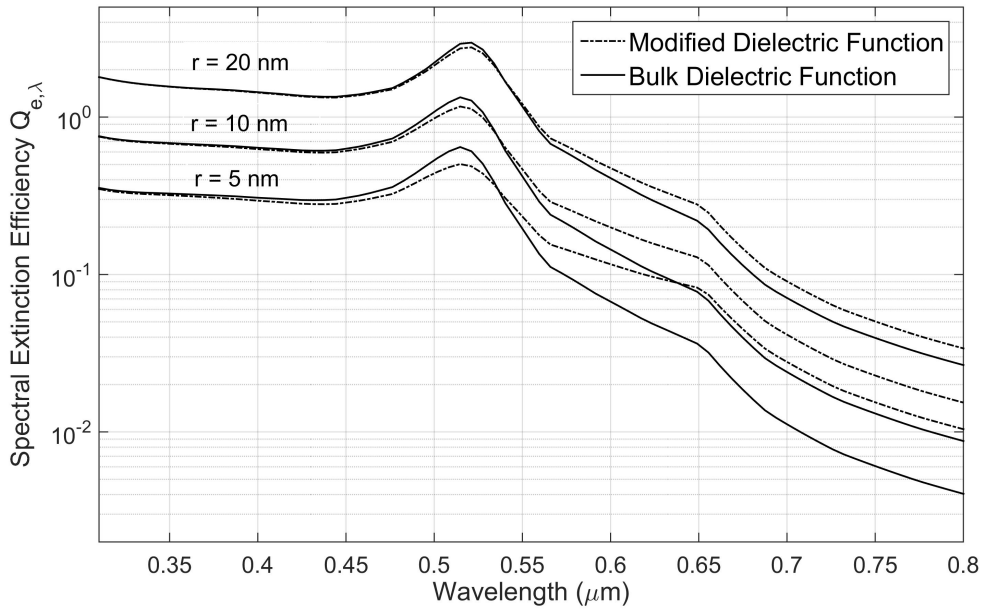

Figure 4.12. Effect of size dependence of the dielectric function on the extinction efficiency of gold nanoparticles with water as base fluid.

4.4.2. Comparison of core-shell nanofluid and pure nanofluid optical properties

The core-shell nanofluid extinction coefficients for silica/gold nanoparticles of total radius 20 nm and shell thicknesses 3 and 5 nm were compared with that of pure gold and graphite nanofluids that are of the same size. Base fluid was water and volume fraction was 0.005% for all nanofluids. Results are shown in Figure 4.13. As the size of the gold shell decreases, the plasmonic peak is significantly red-shifted, and this effect is much more pronounced than that is observed for pure nanoparticles in Subsection 4.4.1. Height of the plasmonic peak of core-shell nanofluids is seen to be higher and broader than pure nanoparticles.

Since the spectral nature of the incident solar radiation is a defining characteristic of the problem considered, the size dependence of the optical behavior of nanoparticles turns out to be a crucial factor in the modelling of their radiative properties.

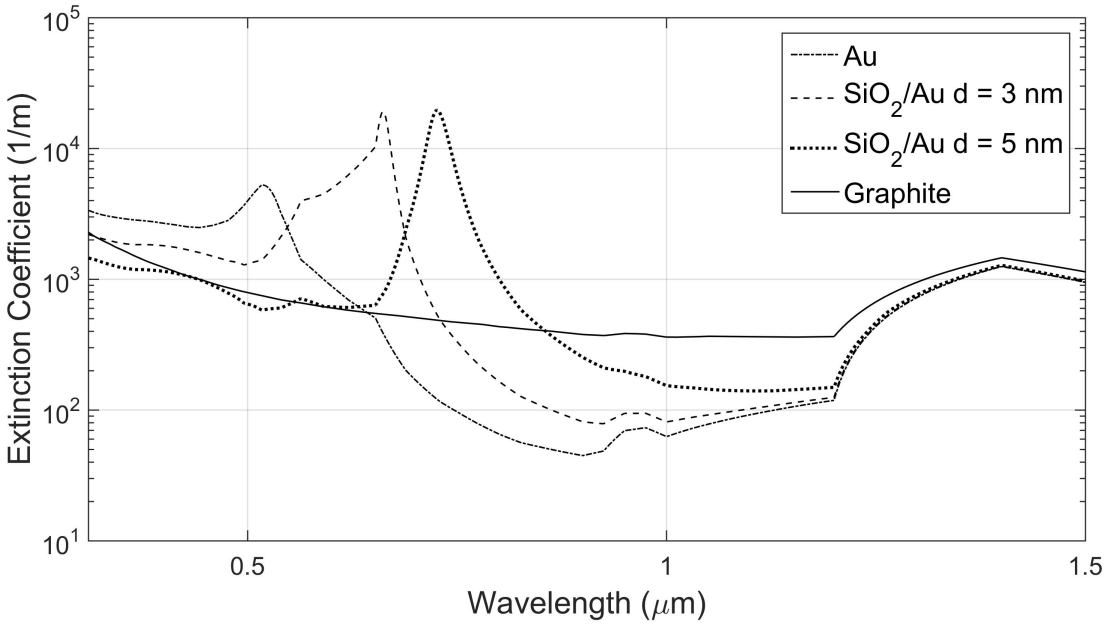

Figure 4.13. Extinction coefficient comparison of core-shell and pure nanoparticle nanofluids (water, 0.005%).

4.4.3. Volume fraction effect on optical properties

Optical properties of nanofluids with three different volume fractions are shown in Figure 4.14. All three cases of nanofluids shown here has gold nanoparticles with 20 nm radius and water as base fluid. Increased volume fractions of nanoparticles result in higher extinction coefficient values for nanofluids. This behaviour is expected, since increased number of particles means higher rates of absorption and scattering. Whereas the effect of volume fraction on optical properties is obvious, its effect on efficiency of the collector system is not straightforward, and is investigated in following sections.

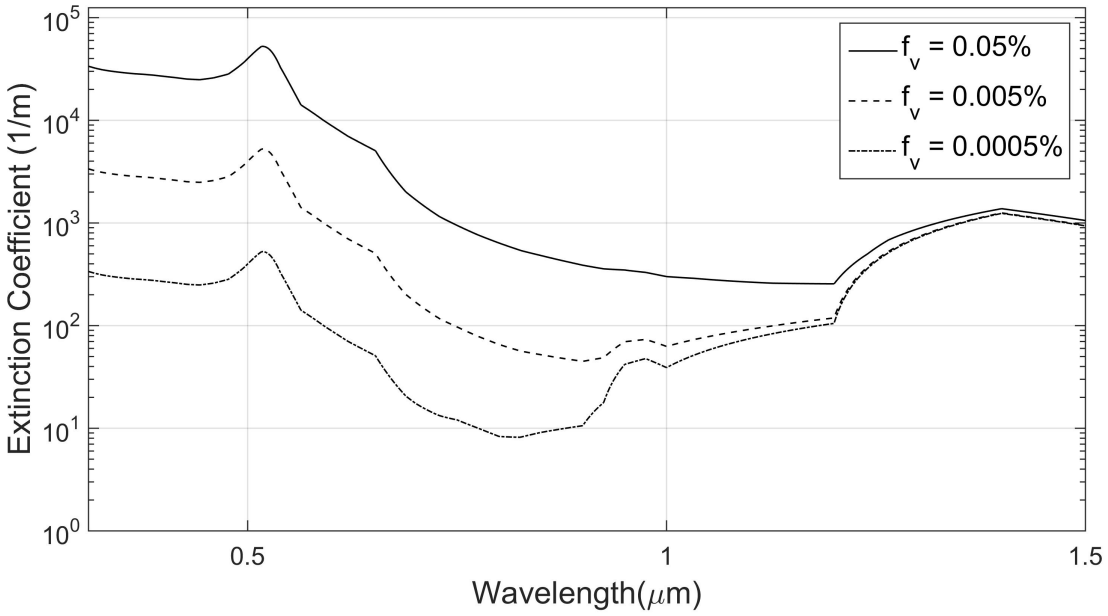

Figure 4.14. Effect of volume fraction on optical properties.

4.5. Results for a Parallel Plate Direct Absorption Collector

Results for core-shell nanofluid with SiO_2-Au nanoparticles (r_{core} = 20 nm, r_{shell} = 25 nm) dispersed in water with a volume fraction of f_v = 0.005% is presented below. In Figure 4.15, separate contributions of the nanoparticle and base fluid spectral extinction coefficients are displayed, along with their sum, which gives the spectral extinction coefficient of the nanofluid. Nanoparticle contribution to the ex-

tinction spectrum is predominantly at the visible range, justifying their use in DASC applications, since most of the energy of incident solar radiation is therein.

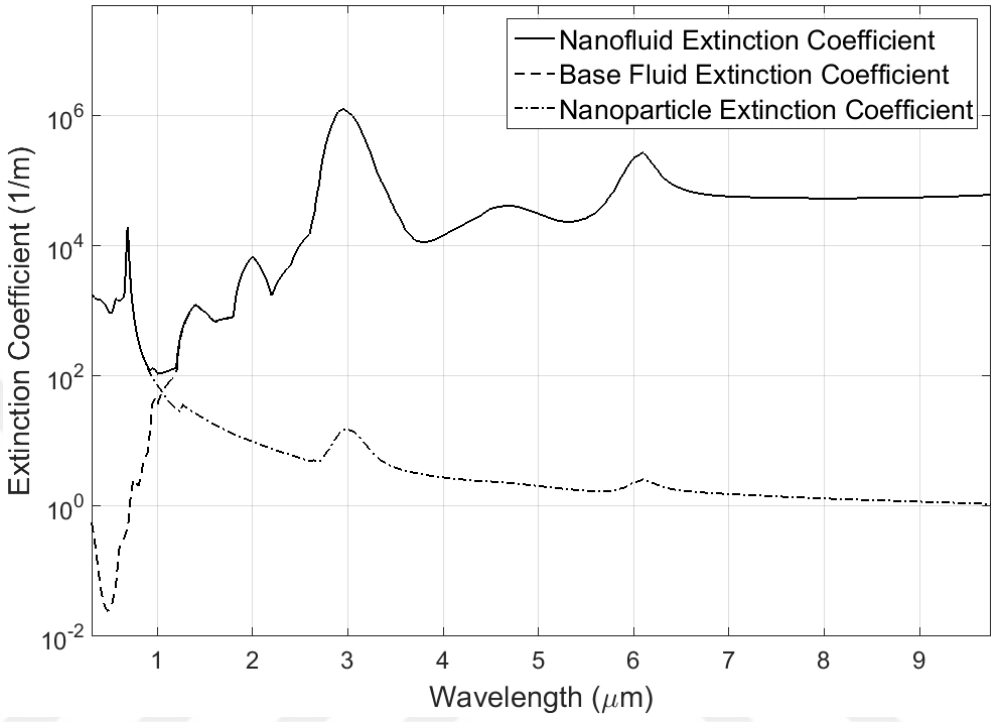

Figure 4.15. Extinction coefficient of SiO_2-Au 20/25 water with 0.005% particle concentration.

The radiative heat flux profiles in Figure 4.16 show the decay of incoming radiation intensity as it penetrates nanofluids with different concentration ratios. All three nanofluids have SiO_2-Au 20/25 nanoparticles and base fluid water. At volume fraction 0.05%, hardly any radiation reaches the bottom plate, and most of the heat is captured in the upper regions of the flow. This leads to the temperature profile in Figure 4.17, where higher temperature regions are seen to be close to the glass cover at the top. This effect increases convective heat loss, which is the main source of heat loss for the system considered in this study, similar to the conventional flat plate collectors, where heat loss occurs mainly from the top via the absorber plate.

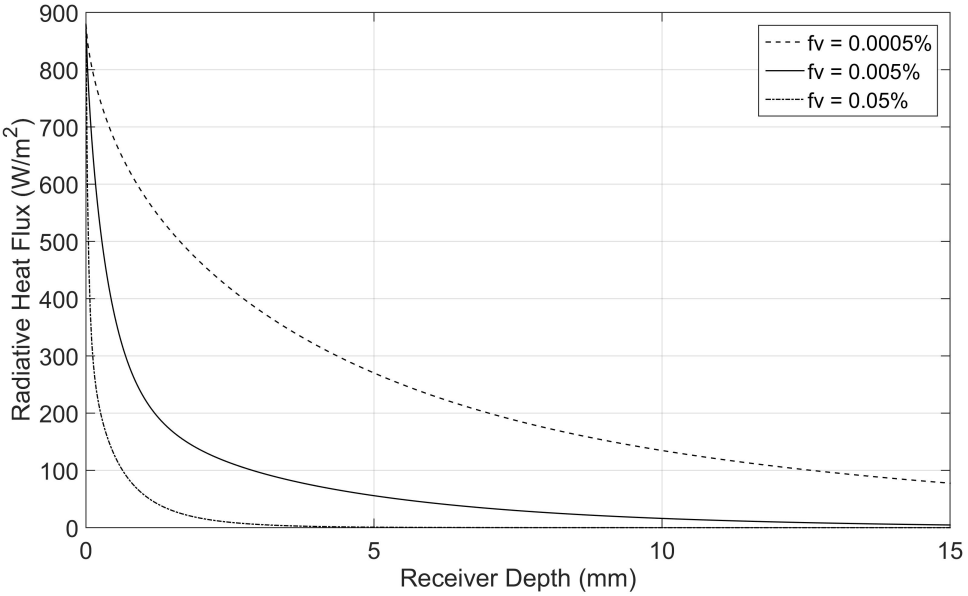

Figure 4.16. Radiative heat flux for SiO_2-Au 20/25 nm water with various particle concentrations.

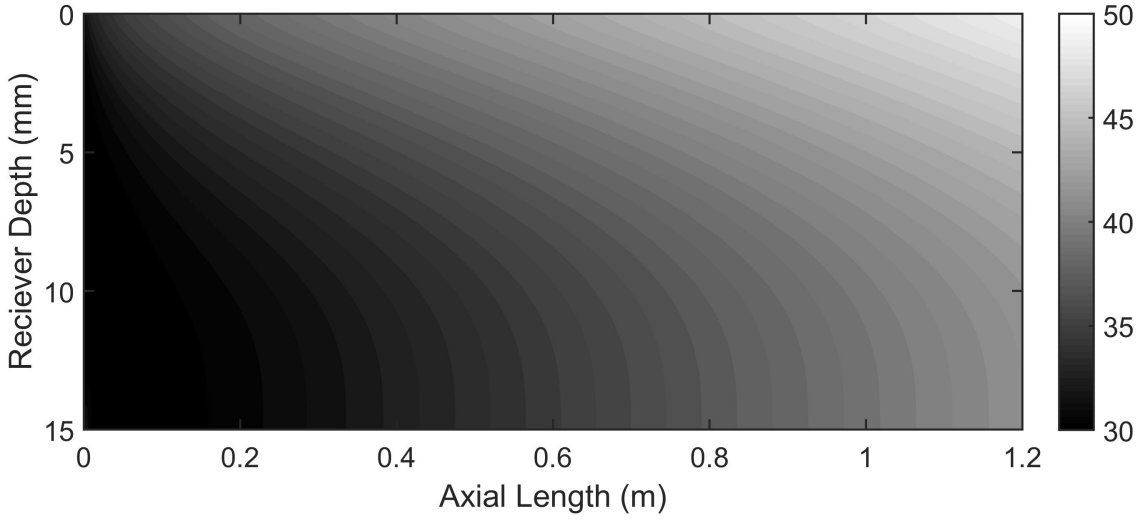

Figure 4.17. Temperature profile for SiO_2-Au 20/25 water with 0.05% particle concentration.

4.5.1. Thermal performance effects of volume fraction

Since the volume fraction has a direct influence on the optical properties of nanofluids, it also impacts on the thermal performance of the collector. Higher overall extinction values result in the concentration of radiation at the upper layers of the flow. Lower volume fractions allow the incident solar radiation to penetrate deeper in to the nanofluid, resulting in a more uniform rise in temperature. At low particle loadings radiative heat flux at the lower end of the receiver is usually non-zero, and it is absorbed and transferred to the nanofluid by the absorber plate, heating the lower region of the flow. These two factors result in a more uniform heating of the nanofluid and eliminates high surface temperature, which are often the case for high volume fractions. The influence of volume fraction on the temperature profile is shown in Figures 4.17 and 4.18, which correspond to 0.05% and 0.0005% respectively. Both cases are nanofluids with base fluid water and silica core and gold shell nanofluids with size 25 nm total radius and 5 nm shell thickness.

Temperature values rise up to 49°C for the 0.05% case, whereas the maximum temperature for 0.0005% is around 46°C. The latter case also shows a more even temperature rise along the collector's length. Total convective heat losses calculated for the two cases were 186.7 W/m^2 for 0.0005% and 210.8 W/m^2 for 0.05%; about 13% more for the higher volume fraction nanofluid. As expected the mean exit temperature of the 0.0005% nanofluid ($44.1°C$) is higher than that of the 0.05% one ($43.4°C$).

4.5.2. Efficiency of the Collector System

The main performance metric considered for the collector model is the total efficiency defined by Equation 3.1. This term characterizes total energy gain by the system compared to the incident solar radiation. While convective heat loss is the main factor that reduces total efficiency, another important factor is the backscattering of radiation, which leads radiation loss. The combination of both large particle sizes, at which scattering becomes prominent, and high volume fractions, significantly lower the total efficiency. Dominant scattering contribution can be seen in Figure 4.19, where

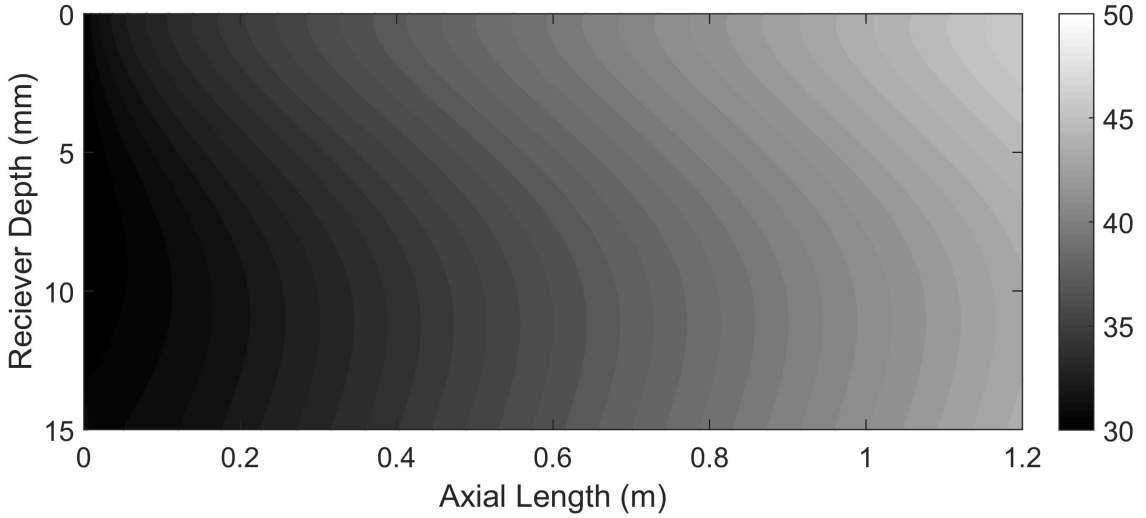

Figure 4.18. Temperature profile for SiO_2-Au 20/25 water with 0.0005% particle concentration.

the extinction, absorption and scattering efficiencies of a gold nanoparticle with 50 nm radius in water is shown. The ratio of energy loss due to backscattering can be quantified by using the upper and lower hemispherical intensity profiles obtained from the solution of the Two-Flux equations (Equations 2.7 and 2.6). For gold nanofluid with volume fraction 0.01% and 50 nm radius, q_r^+, q_r^- and $q_r = q_r^+ - q_r^-$ are shown in 4.21, along with the result of radiative heat flux calculated using Beer-Lamber law. Intensity values for the same case is shown in Figure 4.20. Beer-Lambert law is an exponential decay law for intensity distribution for an absorbing medium. It has the following equation for the intensity [38]:

$$\frac{dI_\lambda}{dy} = -\beta_\lambda(y) I_\lambda \tag{4.9}$$

The value of q^- at $y = 0$ gives the amount of radiation lost to the environment, and for this case it amounts to approximately 25% of the incoming solar radiation. Since Beer-Lambert law incorporates scattering into its formulation only in the extinction term, it can not show the backscattering behavior observed in the Two-Flux formulation. Because of this, Beer-Lambert Law overestimates the flux distribution considerably

leading to an overestimation of about 180 W/m^2 in terms of maximum flux value (888 W/m^2 for Beer-Lambert law and 709 W/m^2 for Two-Flux approximation). Therefore, for nanofluids where scattering is important, Beer-Lambert law is not an accurate model.

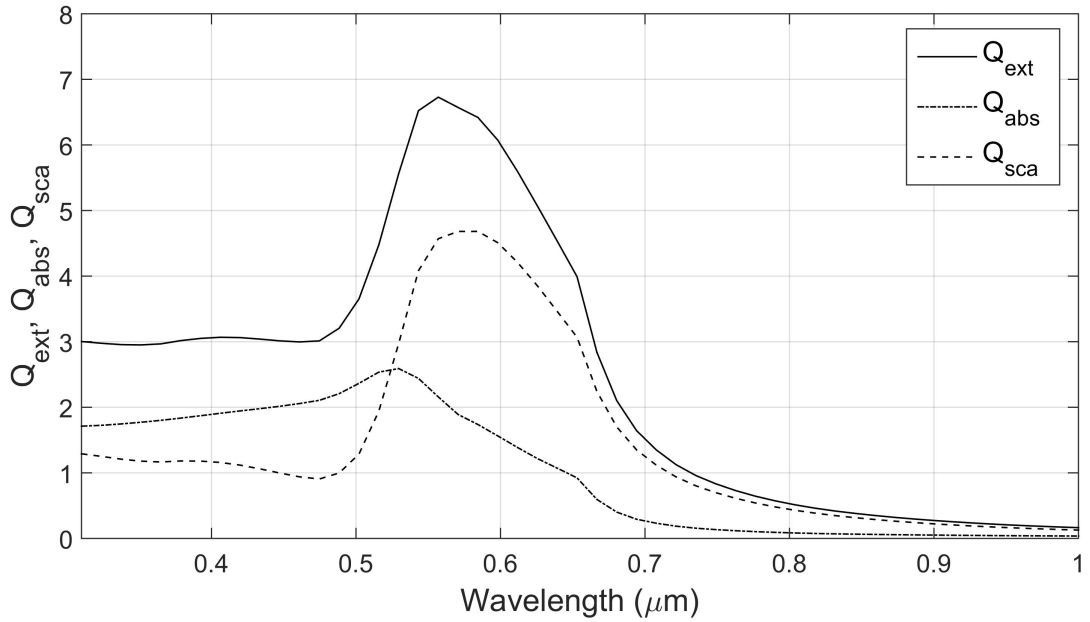

Figure 4.19. Optical efficiency factors for a gold nanoparticle with a radius of 50 nm in water.

4.5.3. Effect of Flow Velocity

Since the main goal of this study is to compare nanofluid performances, simulations were conducted using a single flow velocity value. However it is still important to consider its effect on collector efficiency. Results for different velocity values are depicted in Figure 4.22. The nanofluid considered was water with 20 nm graphite nanoparticles and a volume fraction of 0.005%. An increase in flow velocity leads to higher efficiency values; however, this trend approaches an asymptotic value after which total efficiency values are effectively the same. It is worth noting that increased efficiency comes at the cost of significantly reduced ΔT. Such low ΔT would require many cycles to heat the nanofluid and would also require significant pumping power

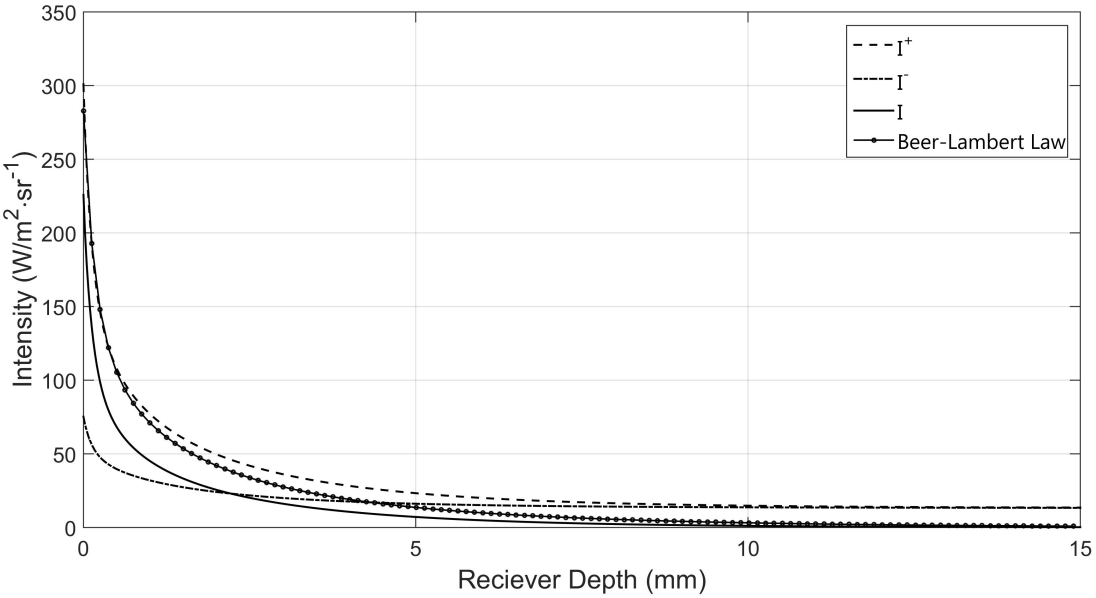

Figure 4.20. Effect of backscattering and comparison of Two-Flux method and Beer-Lambert Law, 50 nm gold nanoparticles in water, 0.01% volume fraction.

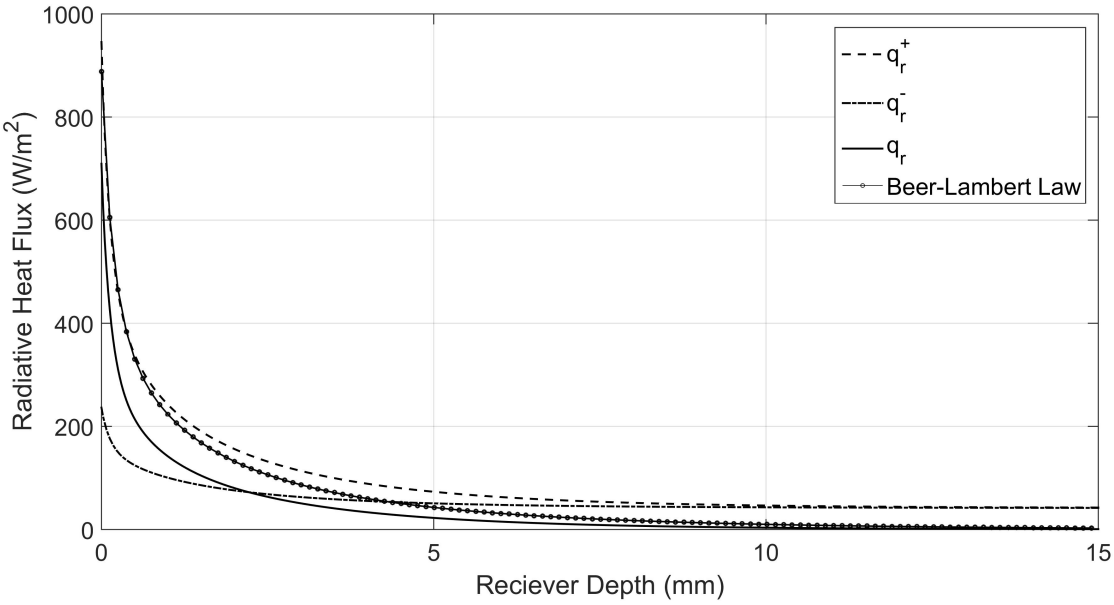

Figure 4.21. Effect of backscattering and comparison of Two-Flux method and Beer-Lambert Law, 50 nm gold nanoparticles in water, 0.01% volume fraction.

to achieve high mass flow rates, rendering it impractical.

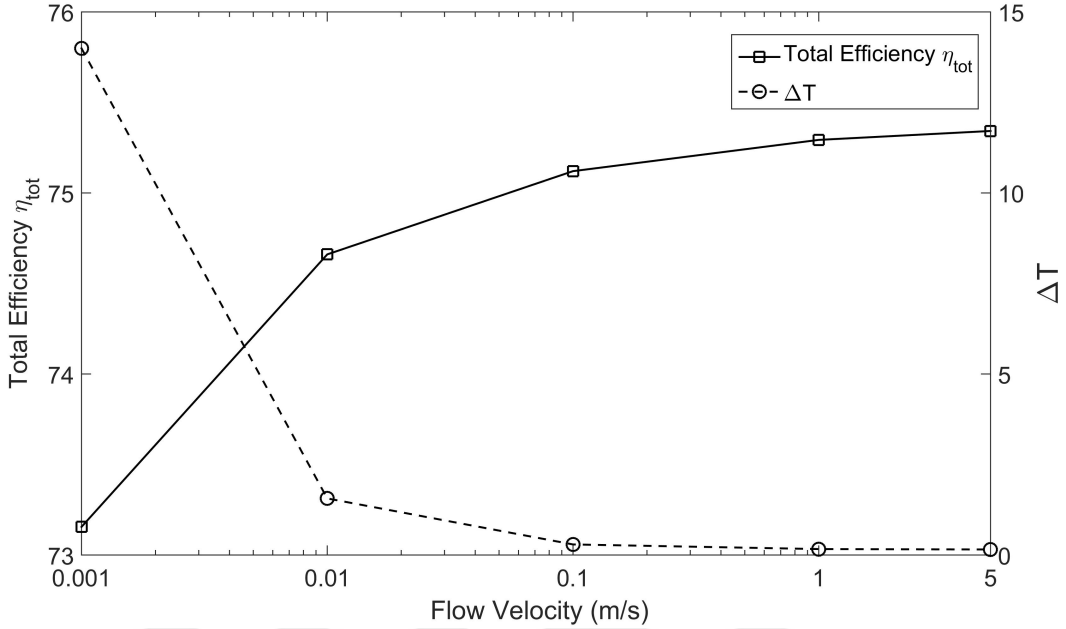

Figure 4.22. Effect of flow velocity on total efficiency and ΔT, 20 nm graphite water nanofluid with volume fraction 0.005%.

4.5.4. Base Fluid Comparison

Base fluids considered in this study were water and ethylene glycol (EG). In all cases, nanofluids with water as base fluid showed higher total efficiencies. As an example, efficiency of two different nanofluids with different base fluids and SiO_2/Au core-shell nanoparticles with 5 nm shell thickness and various total sizes are shown in Figures 4.23 and 4.24. The general trends are quite similar, the efficiency values for EG nanofluids are 4-5 % lower than those of water nanofluids. This is mainly due to two factors: the inferior infrared absorption properties, and low specific heat and density of EG with respect to water. The second factor yields higher temperatures and lower mass flow rates at a given flow velocity, increasing total convective heat loss, and decreasing amount of heat the EG nanofluid can absorb.

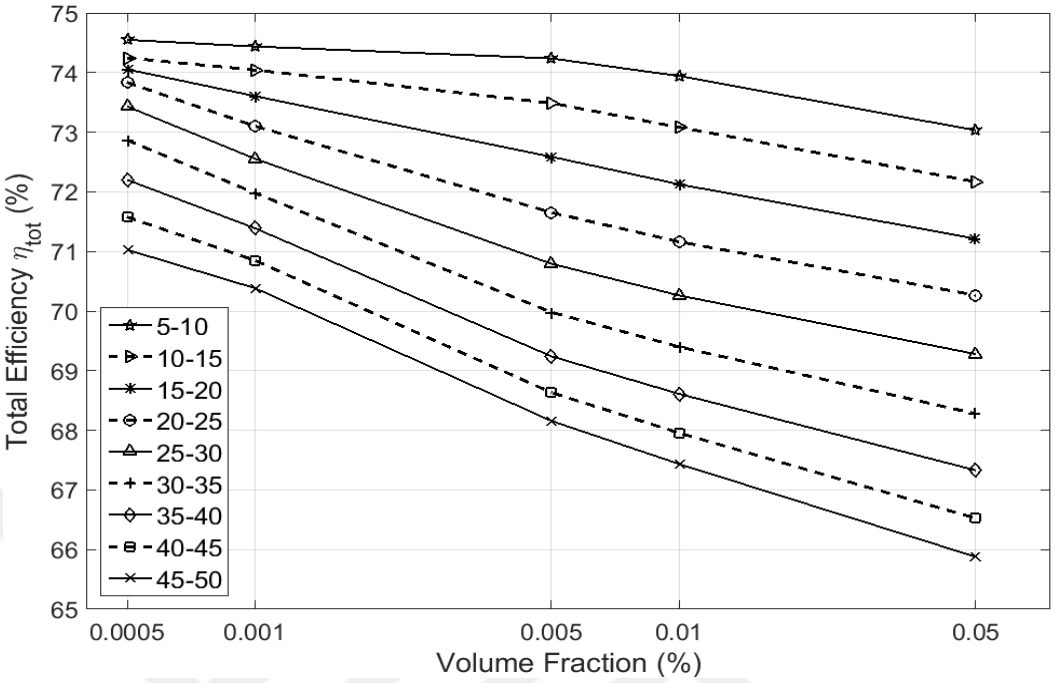

Figure 4.23. Total efficiency values for water based SiO_2/Au nanofluid with shell thickness of 5 nm.

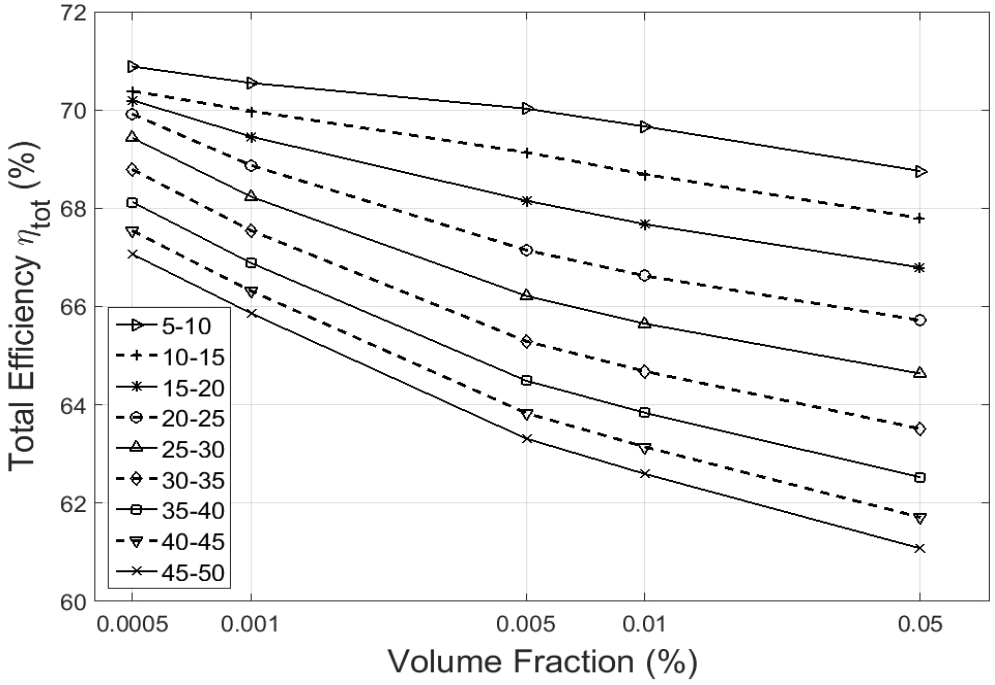

Figure 4.24. Total efficiency values for EG based SiO_2/Au nanofluid with shell thickness of 5 nm.

In order to better understand the peak behavior of total efficiency that nanofluids exhibit two more volume fraction values of 0.00025% and 0.0001% were investigated for nanofluids with base fluid water. Results showed that the graphite nanofluid with particle size $r = 5nm$ and $f_v = 0.0005\%$ gives highest total efficiency value of 76.2%. Results for this case are shown in Figure 4.25. The trend seen here is shared with most of the pure nanofluids, with efficiency decreasing at higher volume fractions, and efficiency increasing with smaller particle sizes. These two phenomena are due to previously mentioned effects of concentration of radiative intensity at the top leading to more convective losses and backscattering due to increased scattering behavior of nanoparticles respectively.

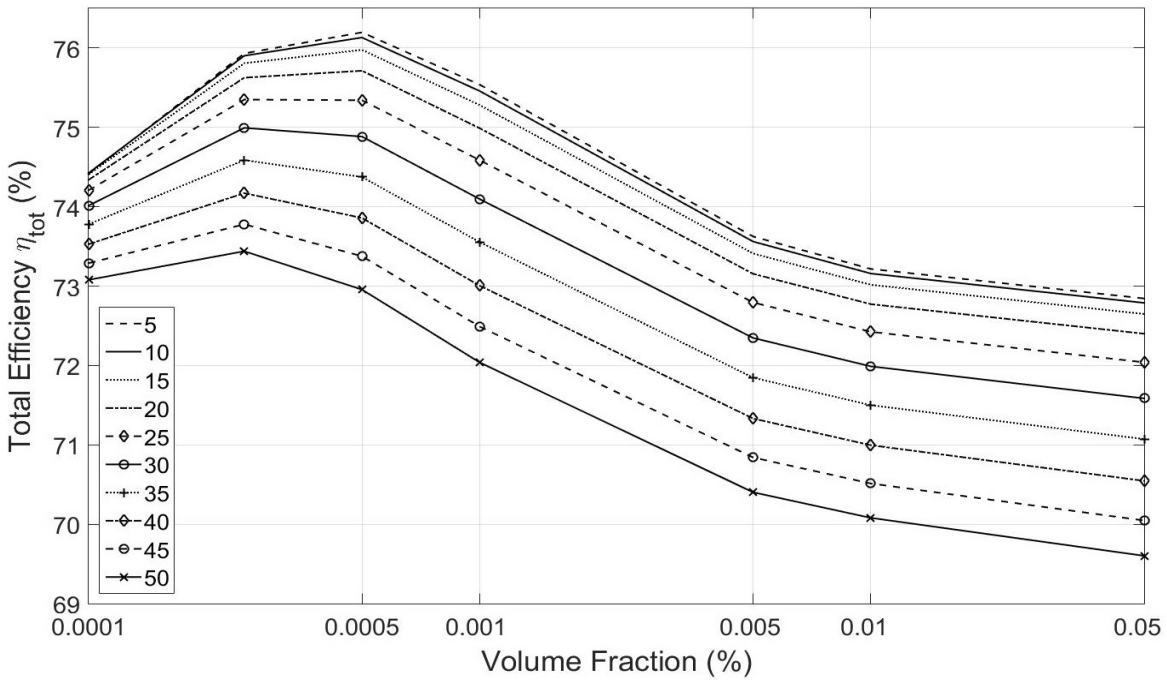

Figure 4.25. Total efficiency of graphite nanofluids with base fluid water.

Results show that each nanofluid has a peak value for total efficiency, and the volume fraction value at which this peak occurs differs from one nanofluid to another. The efficiency curves for the core-shell nanofluid with Silica/Silver nanoparticles of 3 nm shell thickness, dispersed in water,is shown in Figure 4.26. In order to investigate the cause of this trend, change of absorption and flow efficiency with respect to volume fraction is inspected. The absorption efficiency increases with increased volume frac-

tions and flow efficiency consequently decreases. The volume fraction at which their product is greatest corresponds to the peak of the total efficiency curve. The three efficiencies for another case without a peak in the selected range is depicted in Figure 4.28. This case shows nearly constant absorption efficiency, which can be explained by the optimal amount of absorption and backscattering leading to maximum absorption efficiency. While the absorption efficiency does not change significantly with lower volume fractions, flow efficiency increases at a considerably faster rate. This gives rise to higher overall efficiency as volume fraction decreases. With even more dilute nanofluids, absorption losses are expected to increase due to incident radiation being reflected from the lower plate and not being absorbed by the nanofluid before it escapes the receiver. This will in turn result in a drop in total efficiency values.

To demonstrate this for the case of graphite nanofluids, efficiency values for 5 nm graphite nanofluid with base fluid water with a larger range of volume fractions is show in Figure 4.29. The dashed line represents the total efficiency of pure water, which is 71.3%. Volume fractions up to two orders of magnitude smaller were also included to confirm that the results tend to the efficiency value for pure water in the limit. Just like the core-shell nanofluid mentioned above, there is a peak value for total efficiency. This means that this peak behavior can be observed in all nanofluids and is related to the absorption and flow efficiencies. Maximum efficiency is achieved near volume fraction of 0.0005% after which the efficiency drops again. More generally for each nanofluid case, the volume fraction value where the sum of radiative and convective losses are smallest has the highest total efficiency value.

In terms of nanoparticle materials, Aluminium core-shell nanofluids exhibit similar performance to gold and silver core-shell nanofluids. The efficiency plots for 3 and 5 nm shell thickness silica-aluminium are presented in Figure 4.30. Copper core-shell nanofluid performance is depicted in Figure 4.31. Copper core-shell nanofluids show peaks at lower volume fractions overall compared to other core-shell nanofluid types.

One possible advantage of core-shell nanofluids is that the cores of their constituent nanoparticles, made of silica, means considerably less expensive metals are

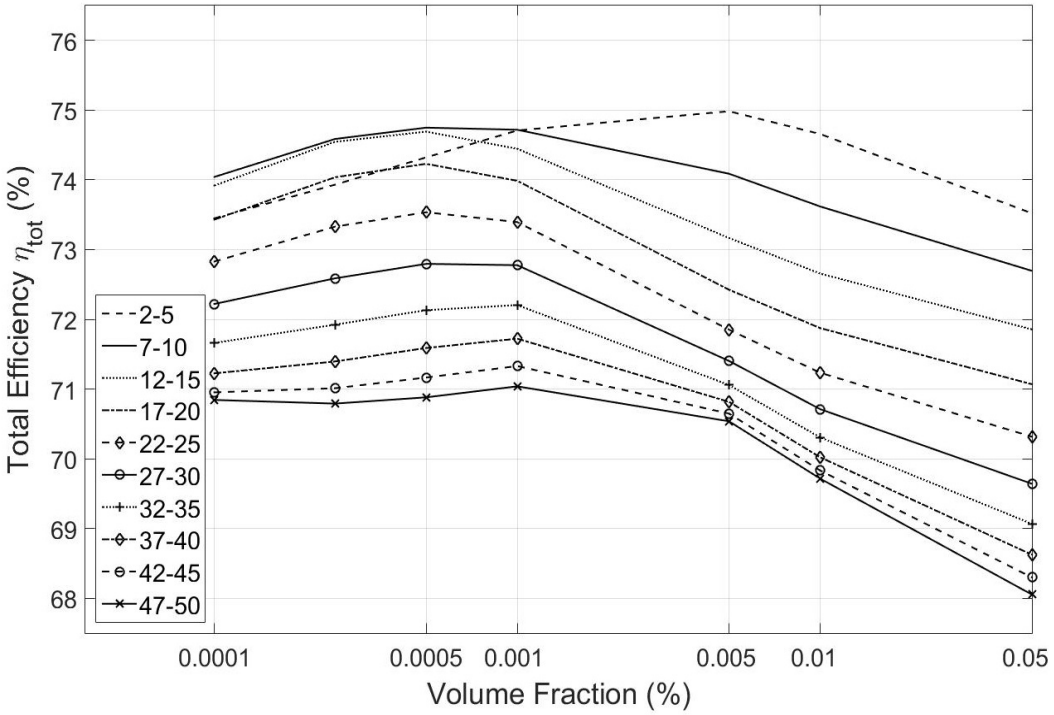

Figure 4.26. Total efficiency of SiO_2/Ag 3 nm shell thickness water nanofluid.

required in their production. Thus it is worth comparing their performance to their pure metal nanoparticle counterparts. Efficiency results show that for aluminium, gold and copper, performance is generally slightly higher for core-shell nanofluids; whereas for silver, opposite is true. As with the case of silica-copper nanofluids, core-shell nanofluids at small sizes exhibit peak efficiency values at lower volume fractions, which is advantageous since it reduces the amount of nanoparticles required to produce the nanofluid. Total efficiency results for pure nanofluids are located Appendix A.

Performance-wise, core-shell nanofluids are close to but outperformed by graphite nanofluids. It is worth noting that peak total efficiencies at higher volume fractions also mean increased nanofluid cost, and this is one of the main reasons graphite nanofluids seem to be more favourable in the scope of this model. Core-Shell nanofluids with particle shell thickness of 3 nm performed better than 5 nm ones while the latter was also surpassed by their pure counterparts. Pure nanofluids also showed similar results, with bigger particle size leading to lower total efficiency in general. In fact

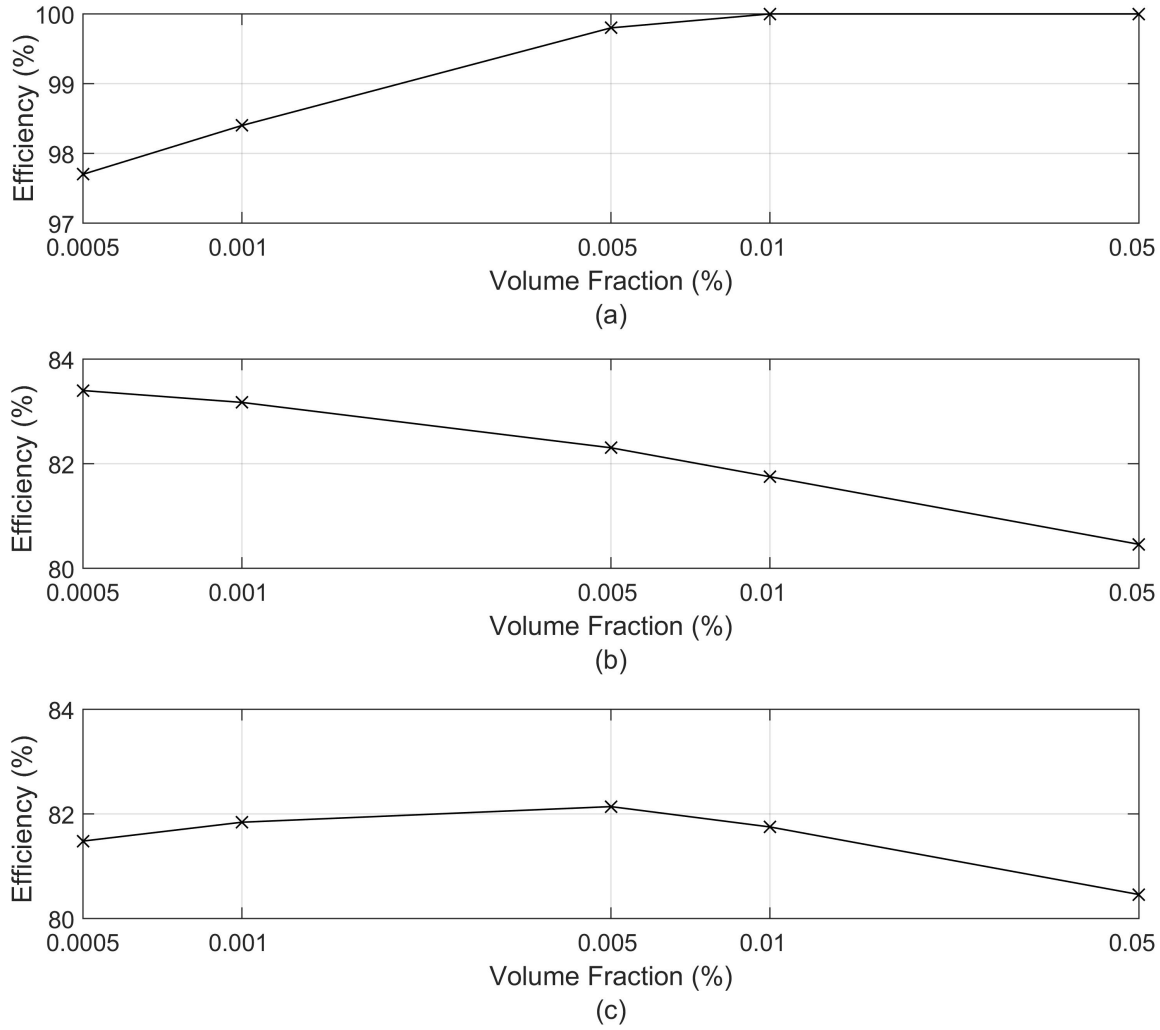

Figure 4.27. Water with SiO_2-Ag nanoparticles of 5 nm size and 3 nm shell thickness; results for (a) Absorption Efficiency (b) Flow efficiency (c) Product of absorption and flow efficiencies.

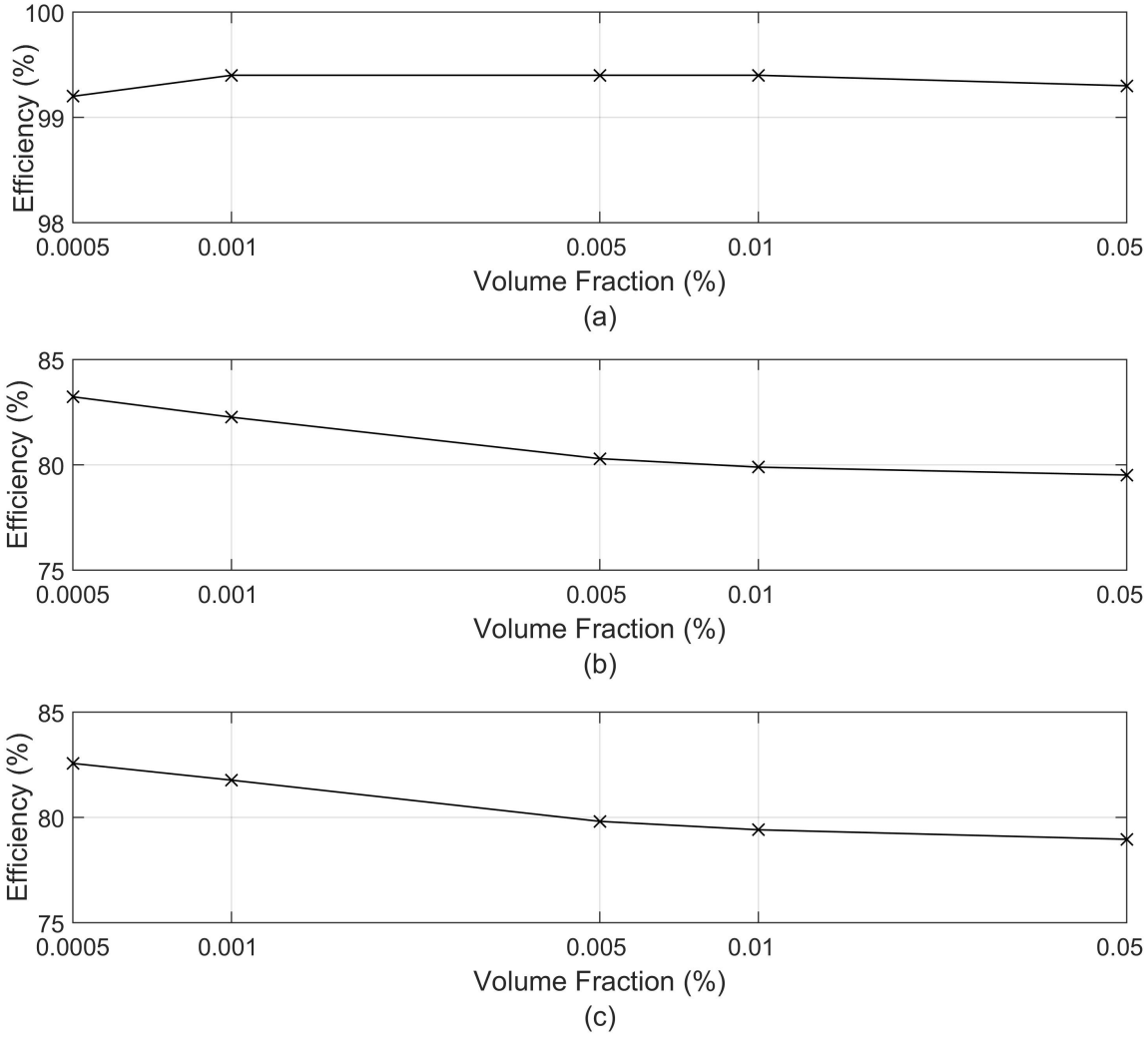

Figure 4.28. Water/Graphite 25 nm results for (a) Absorption efficiency (b) Flow efficiency (c) Product of absorption and flow efficiencies.

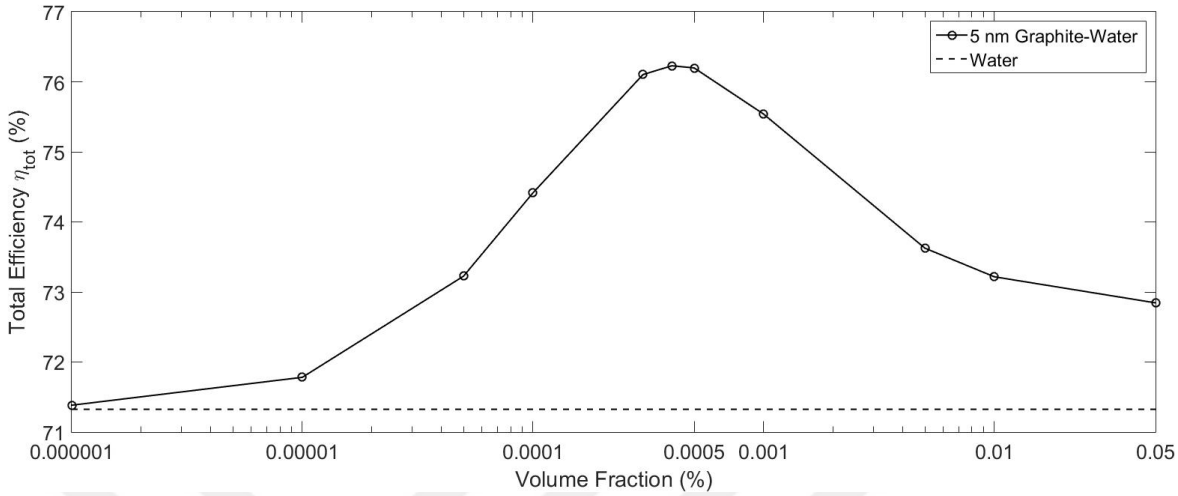

Figure 4.29. Comparison of volume fraction for graphite water nanofluid with 5 nm particle size.

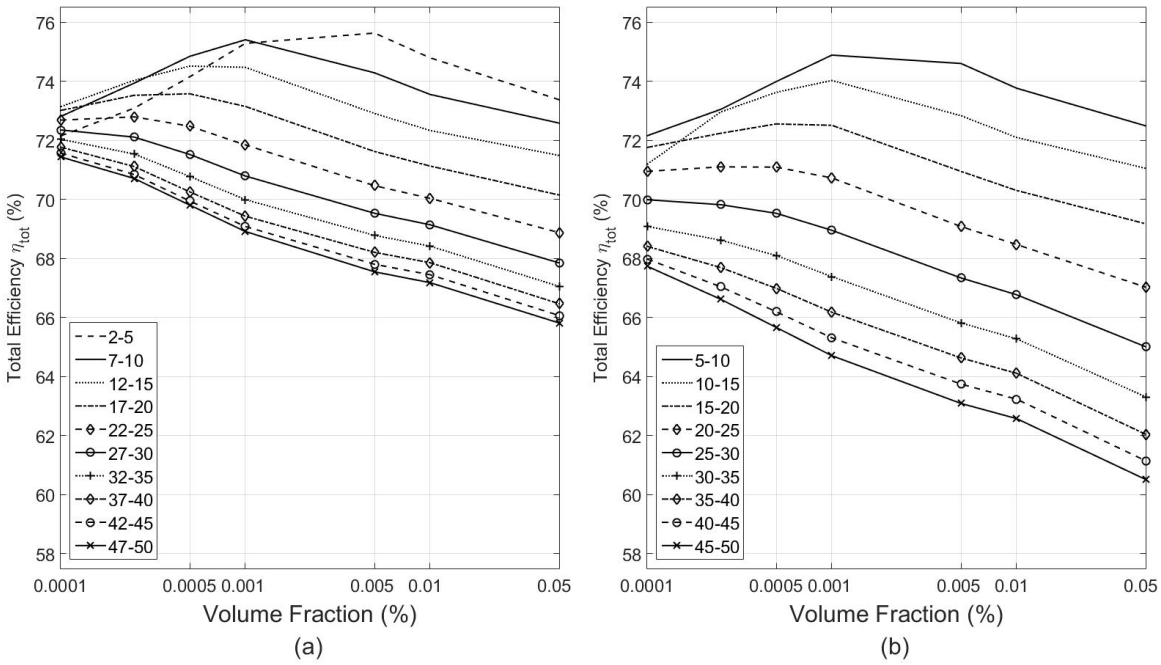

Figure 4.30. Total efficiency results for water SiO_2-Al nanofluid with shell thickness 3 nm and 5 nm.

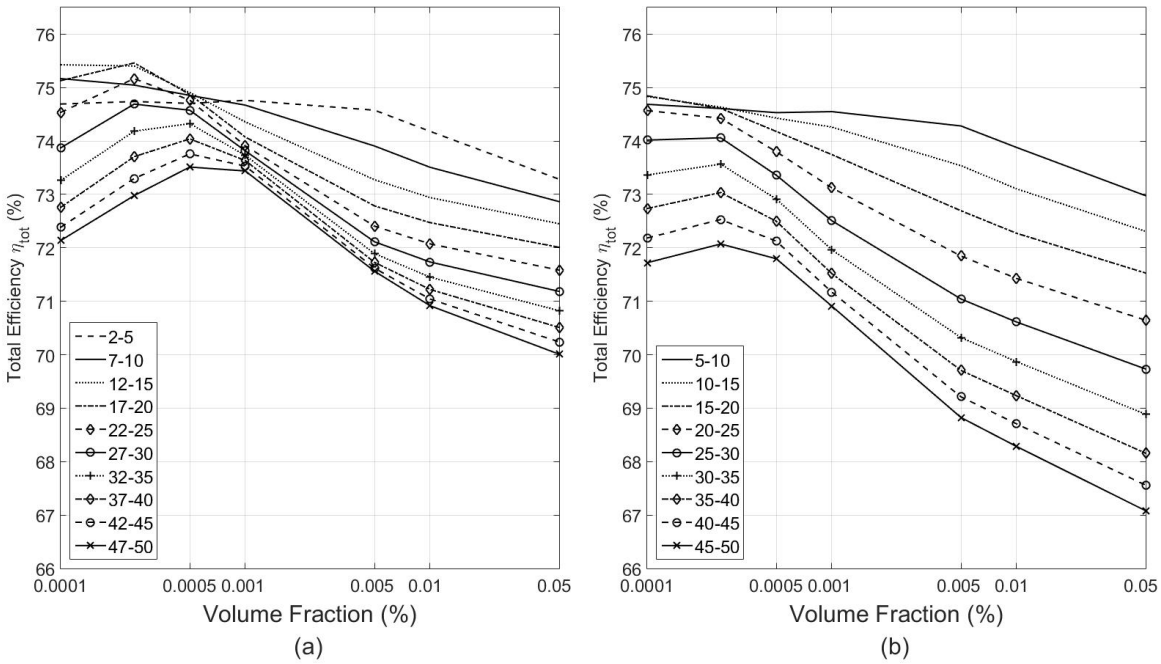

Figure 4.31. Total efficiency results for water SiO_2-Cu nanofluid with shell thickness 3 nm and 5 nm.

total efficiency is much more lower for nanofluids with large pure particles, compared to core-shell and graphite nanofluids of same nanoparticle radii.

5. CONCLUSIONS AND FUTURE WORK

5.1. Conclusions

Nanofluids for use in Direct Absorption Solar Collectors were investigated with a simplified 2D model. Radiative properties were computed using Lorenz-Mie theory and its variations to implement size effects were implemented. The effect of particle volume fraction, base fluid, nanoparticle material and size on efficiency is investigated considering combined convection-radiation heat transfer. Core-shell nanoparticles with silica core and gold, silver, copper and aluminium shell were compared with their pure counterparts and also graphite.

Base fluids considered were water and ethylene glycol (EG) and water outperformed EG in all cases. This performance difference can be attributed to higher thermal inertia and also significantly better infrared absorption properties of water. The latter is especially important since incident solar radiation contains an non-negligible amount of infrared radiation which cannot be captured by EG nanofluids.

Graphite nanofluids with water as base fluid achieved the highest total efficiency value and were slightly better than both core-shell and pure nanofluids. Overall, the efficiency difference between graphite and other nanofluids were quite small, however in terms of application considerations, graphite would be the best candidate for flat plate Direct Absorption Solar Collectors, in terms of both material cost and performance with respect to other nanofluid types. Compared to conventional flat plate collectors, our model shows that nanofluid based collectors show an improvement of up to 15% in total efficiency.

It was also observed that nanofluids show peaks at different volume fraction rates. This was shown to be related to the combined effect of both the absorption and flow efficiencies.

Results also showed that a balance between radiative losses (backscattering and reflected radiation from the bottom plate escaping the receiver), and convective heat loss is required to obtain maximum total efficiency.

5.2. Recommendations for Future Work

The model used in this study assumed fixed geometry and flow parameters were kept constant. An optimization study is possible, in terms of geometry and flow conditions, in order to maximize nanofluid performance.

Other types of solar collector systems may also benefit from the use of nanofluids. These include Parabolic Trough Collectors among others. Use of nanofluids in such systems along with their overall performance including heat exchanger and storage performances is another research opportunity. Since these systems involve high temperature it is also important to investigate which base fluids would be suitable. In particular molten salts (ionic liquids) show promise, due to their high temperature range as well as heat storage ability. Stability of nanofluids at high temperatures is also an relevant research topic for use in such applications.

There have also been studies of different carbon-based materials used as nanoparticles in nanofluids including Single- and Multi-Walled Carbon Nanotubes and Graphene. Such nanofluids can be investigated for use in DASC systems and their performance compared to graphite nanofluids. A significant challenge, and research opportunity, is the optical property modelling of these nanoparticles, which are quite different than the spherical geometry usually associated with spherical nanoparticles.

REFERENCES

1. Solomon, S., *Climate change 2007-the physical science basis: Working group I contribution to the fourth assessment report of the IPCC*, Vol. 4, Cambridge University Press, 2007.

2. US Energy Information Administration, "Annual energy outlook 2013", 2013.

3. Chu, Y., "Review and comparison of different solar energy technologies", *Global Energy Network Institute (GENI), San Diego, CA*, 2011.

4. Wasfi, M. and S. Member, "Solar Energy and Photovoltaic Systems", *Cyber Journals: Multidisciplinary Journals in Science and Technology, Journal of Selected Areas in Renewable and Sustainable Energy (JRSE)*, Vol. 1, No. 2, pp. 1–8, 2011.

5. International Energy Agency, "Technology Roadmap: Solar Photovoltaic Energy", 2014.

6. O'Regan, B. and M. Grätzel, "A low-cost, high-efficiency solar cell based on dye-sensitized colloidal TiO2 films", *nature*, Vol. 353, No. 6346, pp. 737–740, 1991.

7. Bai, Y., Y. Cao, J. Zhang, M. Wang, R. Li, P. Wang, S. M. Zakeeruddin, and M. Grätzel, "High-performance dye-sensitized solar cells based on solvent-free electrolytes produced from eutectic melts", *Nature materials*, Vol. 7, No. 8, pp. 626–630, 2008.

8. Kuravi, S., J. Trahan, D. Y. Goswami, M. M. Rahman, and E. K. Stefanakos, "Thermal energy storage technologies and systems for concentrating solar power plants", *Progress in Energy and Combustion Science*, Vol. 39, No. 4, pp. 285–319, 2013.

9. Zhang, H., J. Baeyens, J. Degrève, and G. Cacères, "Concentrated solar power

plants: Review and design methodology", *Renewable and Sustainable Energy Reviews*, Vol. 22, pp. 466–481, 2013.

10. Barlev, D., R. Vidu, and P. Stroeve, "Innovation in concentrated solar power", *Solar Energy Materials and Solar Cells*, Vol. 95, No. 10, pp. 2703–2725, 2011.

11. Fernández-García, A., E. Zarza, L. Valenzuela, and M. Pérez, "Parabolic-trough solar collectors and their applications", *Renewable and Sustainable Energy Reviews*, Vol. 14, No. 7, pp. 1695–1721, 2010.

12. Price, H., E. Lupfert, D. Kearney, E. Zarza, G. Cohen, R. Gee, and R. Mahoney, "Advances in parabolic trough solar power technology", *Journal of Solar Energy Engineering*, Vol. 124, No. 2, pp. 109–125, 2002.

13. Kalogirou, S. A., "Solar thermal collectors and applications", *Progress in energy and combustion science*, Vol. 30, No. 3, pp. 231–295, 2004.

14. Y., T. and Z. C. Y., "A review of solar collectors and thermal energy storage in solar thermal applications", *Applied Energy*, Vol. 104, pp. 538–553, 2013.

15. Tina, G., M. Rosa-Clot, P. Rosa-Clot, and P. Scandura, "Optical and thermal behavior of submerged photovoltaic solar panel: SP2", *Energy*, Vol. 39, No. 1, pp. 17–26, 2012.

16. Khullar, V. and H. Tyagi, "Application of nanofluids as the working fluid in concentrating parabolic solar collectors", *37th National & 4th International Conference on Fluid Mechanics & Fluid Power, IIT Madras, Chennai, India, Dec*, pp. 16–18, 2010.

17. Choi, S. U. S., "Enhancing thermal conductivity of fluids with nanoparticles", *Proceedings of the 1995 ASME International Mechanical Engineering Congress and Exposition*, Vol. 231, pp. 99–105, ASME, 1995.

18. Kleinstreuer, C. and Y. Feng, "Experimental and theoretical studies of nanofluid thermal conductivity enhancement: a review.", *Nanoscale research letters*, Vol. 6, No. 1, p. 439, 2011.

19. Kakac, S. and A. Pramuanjaroenkij, "Review of convective heat transfer enhancement with nanofluids", *International Journal of Heat and Mass Transfer*, Vol. 52, No. 13, pp. 3187–3196, 2009.

20. Murshed, S. M. S., K. C. Leong, and C. Yang, "Thermophysical and electrokinetic properties of nanofluids - A critical review", *Applied Thermal Engineering*, Vol. 28, No. 17-18, pp. 2109–2125, 2008.

21. Mahian, O., A. Kianifar, S. A. Kalogirou, I. Pop, and S. Wongwises, "A review of the applications of nanofluids in solar energy", *International Journal of Heat and Mass Transfer*, Vol. 57, No. 2, pp. 582–594, 2013.

22. Otanicar, T., J. Hoyt, M. Fahar, X. Jiang, and R. A. Taylor, "Experimental and numerical study on the optical properties and agglomeration of nanoparticle suspensions", *Journal of Nanoparticle Research*, Vol. 15, No. 11, p. 2039, October 2013.

23. Taylor, R. A., P. E. Phelan, R. Adrian, R. Prasher, and T. P. Otanicar, "Nanofluid Extinction Coefficients for Photothermal Energy Conversion", *ASME/JSME 2011 8th Thermal Engineering Joint Conference*, pp. T30073–T30073, American Society of Mechanical Engineers, 2011.

24. Moreira, L. M., E. Carvalho, M. Bell, V. Anjos, A. Sant'Ana, A. P. P. Alves, B. Fragneaud, L. Sena, B. Archanjo, and C. Achete, "Thermo-optical properties of silver and gold nanofluids", *Journal of thermal analysis and calorimetry*, Vol. 114, No. 2, pp. 557–564, 2013.

25. Otanicar, T., R. A. Taylor, P. E. Phelan, and R. Prasher, "Impact of size and scattering mode on the optimal solar absorbing nanofluid", *ASME 2009 3rd In-*

ternational Conference on Energy Sustainability collocated with the Heat Transfer and InterPACK09 Conferences, pp. 791–796, American Society of Mechanical Engineers, 2009.

26. Mercatelli, L., E. Sani, A. Giannini, P. Di Ninni, F. Martelli, and G. Zaccanti, "Carbon nanohorn-based nanofluids: characterization of the spectral scattering albedo", *Nanoscale Research Letters*, Vol. 7, No. 1, p. 96, 2012.

27. Mercatelli, L., E. Sani, G. Zaccanti, F. Martelli, P. Di Ninni, S. Barison, C. Pagura, F. Agresti, and D. Jafrancesco, "Absorption and scattering properties of carbon nanohorn-based nanofluids for direct sunlight absorbers.", *Nanoscale research letters*, Vol. 6, No. 1, p. 282, 2011.

28. Khullar, V., H. Tyagi, P. E. Patrick, T. P. Otanicar, H. Singh, and R. A. Taylor, "Solar Energy Harvesting Using Nanofluids-Based Concentrating Solar Collector", *Journal of Nanotechnology in Engineering and Medicine*, Vol. 3, No. 3, p. 031003, January 2013.

29. Luo, Z., C. Wang, W. Wei, G. Xiao, and M. Ni, "Performance Improvement of a Nanofluid Solar Collector Based on Direct Absorption Collection (DAC) Concepts", *International Journal of Heat and Mass Transfer*, Vol. 75, pp. 262–271, 2014.

30. Tyagi, H., P. Phelan, and R. Prasher, "Predicted Efficiency of a Low-Temperature Nanofluid-Based Direct Absorption Solar Collector", *Journal of Solar Energy Engineering*, Vol. 131, No. 4, p. 041004, 2009.

31. Kearney, D., U. Herrmann, P. Nava, B. Kelly, R. Mahoney, J. Pacheco, R. Cable, N. Potrovitza, D. Blake, and H. Price, "Evaluation of a molten salt heat transfer fluid in a parabolic trough solar field", *ASME Solar 2002: International Solar Energy Conference*, pp. 293–299, American Society of Mechanical Engineers, 2002.

32. Drotning, W. D., "Optical properties of solar-absorbing oxide particles suspended

in a molten salt heat transfer fluid", *Solar Energy*, Vol. 20, No. 4, pp. 313–319, 1978.

33. Tyagi, H., P. E. Phelan, and R. S. Prasher, "Thermochemical Conversion of Biomass Using Solar Energy: Use of Nanoparticle-Laden Molten Salt as the Working Fluid", *ASME 2009 3rd International Conference on Energy Sustainability collocated with the Heat Transfer and InterPACK09 Conferences*, pp. 405–414, American Society of Mechanical Engineers, 2009.

34. Scaffardi, L. B. and J. O. Tocho, "Size dependence of refractive index of gold nanoparticles", *Nanotechnology*, Vol. 17, No. 5, p. 1309, 2006.

35. Blaber, M. G., M. D. Arnold, and M. J. Ford, "Search for the ideal plasmonic nanoshell: the effects of surface scattering and alternatives to gold and silver", *The Journal of Physical Chemistry C*, Vol. 113, No. 8, pp. 3041–3045, 2009.

36. Lv, W., P. E. Phelan, R. Swaminathan, T. P. Otanicar, and R. A. Taylor, "Multifunctional core-shell nanoparticle suspensions for efficient absorption", *Journal of Solar Energy Engineering*, Vol. 135, No. 2, p. 021004, 2013.

37. Lee, B. J., K. Park, T. Walsh, and L. Xu, "Radiative Heat Transfer Analysis in Plasmonic Nanofluids for Direct Solar Thermal Absorption", *Journal of Solar Energy Engineering*, Vol. 134, No. 2, p. 021009, 2012.

38. Howell, J. R., R. Siegel, and M. P. Menguc, *Thermal Radiation Heat Transfer*, CRC press, Boca Raton, 3rd edition, 2010.

39. Fedorov, A. G. and R. Viskanta, "Radiative transfer in a semitransparent glass foam blanket", *Physics and chemistry of glasses*, Vol. 41, No. 3, pp. 127–135, 2000.

40. Siegel, R., "Transient effects of radiative transfer in semitransparent materials", *International Journal of Engineering Science*, Vol. 36, No. 12-14, pp. 1701–1739,

1998.

41. Modest, M. F., *Radiative heat transfer*, Academic press, Amsterdam, 2nd edition, 2013.

42. Taylor, R., S. Coulombe, T. Otanicar, P. Phelan, A. Gunawan, W. Lv, G. Rosengarten, R. Prasher, and H. Tyagi, "Small particles, big impacts: a review of the diverse applications of nanofluids", *Journal of Applied Physics*, Vol. 113, No. 1, p. 011301, 2013.

43. Bohren, C. F. and D. R. Huffman, "Absorption and scattering of light by small particles", 1983.

44. Quinten, M., *Optical Properties of Nanoparticle Systems: Mie and beyond*, Wiley-VCH Verlag GmbH & Co. KGaA, Weinheim, Germany, January 2011.

45. Henyey, L. G. and J. L. Greenstein, "Diffuse radiation in the galaxy", *Annales d'Astrophysique*, Vol. 3, p. 117, 1940.

46. Kreibig, U. and M. Vollmer, *Optical properties of metal clusters*, Vol. 25, Springer-Verlag Berlin Heidelberg, 1995.

47. Granqvist, H. O., C. G., "Optical Absorption of Ultrafine Metals Spheres with Dielectric Cores", *Zeitschrift für Physik B*, Vol. 51, No. 30, pp. 47–51, 1978.

48. Kachan, S. and A. Ponyavina, "Resonance absorption spectra of composites containing metal-coated nanoparticles", *Journal of Molecular Structure*, Vol. 563, pp. 267–272, 2001.

49. Moroz, A., "Electron mean free path in a spherical shell geometry", *The Journal of Physical Chemistry C*, Vol. 112, No. 29, pp. 10641–10652, 2008.

50. Ashcroft, N. W. and N. D. Mermin, *Solid state physics*, Holt, Rinehart and Winston, 1976.

51. Haynes, W. M. (editor), *CRC handbook of chemistry and physics*, CRC press, 95th edition, 2015.

52. Mätzler, C., "MATLAB Functions for Mie Scattering and Absorption. IAP Research Report", *IAP Research Report*, , No. 11, 2002.

53. Taylor, R. A., P. E. Phelan, T. P. Otanicar, R. Adrian, and R. Prasher, "Nanofluid optical property characterization: towards efficient direct absorption solar collectors", *Nanoscale research letters*, Vol. 6, No. 1, pp. 1–11, 2011.

54. O'Hanley, H., J. Buongiorno, T. McKrell, and L.-w. Hu, "Measurement and Model Validation of Nanofluid Specific Heat Capacity with Differential Scanning Calorimetry", *Advances in Mechanical Engineering*, Vol. 2012, pp. 1–6, 2012.

55. Pal, R., *Electromagnetic, Mechanical, and Transport Properties of Composite Materials*, CRC Press, Boca Raton, 2014.

56. Nagarajan, P., J. Subramani, S. Suyambazhahan, and R. Sathyamurthy, "Nanofluids for solar collector applications: a review", *Energy Procedia*, Vol. 61, pp. 2416–2434, 2014.

57. Sundar, L. S., K. V. Sharma, M. T. Naik, and M. K. Singh, "Empirical and theoretical correlations on viscosity of nano fl uids : A review", *Renewable and Sustainable Energy Reviews*, Vol. 25, pp. 670–686, 2013.

58. Akbari, M., N. Galanis, and A. Behzadmehr, "Comparative analysis of single and two-phase models for CFD studies of nanofluid heat transfer", *International Journal of Thermal Sciences*, Vol. 50, No. 8, pp. 1343–1354, 2011.

59. Kleinstreuer, C., *Two-phase flow: theory and applications*, CRC Press, 2003.

60. Mousavi, M., "Investigation of Single Phase Approximation and Mixture Model on Flow Behaviour and Heat Transfer of a Ferrofluid using CFD Simulation",

Advances in Computational Algorithms and Data Analysis, pp. 495–507, Springer, 2009.

61. Xuan, Y. and Q. Li, "Heat transfer enhancement of nanofluids", *International Journal of Heat and Fluid Flow*, Vol. 21, No. 1, pp. 58–64, 2000.

62. Göktepe, S., K. Atalık, and H. Ertürk, "Comparison of single and two-phase models for nanofluid convection at the entrance of a uniformly heated tube", *International Journal of Thermal Sciences*, Vol. 80, pp. 83–92, 2014.

63. Streed, E. R., J. E. Hill, W. C. Thomas, A. G. D. III, and B. D. Wood, "Results and analysis of a round robin test program for liquid-heating flat-plate solar collectors", *Solar Energy*, Vol. 22, pp. 235–249, 1979.

64. Duffie, J. A. and W. A. Beckman, *Solar Engineering of Thermal Processes*, Wiley New York, 2013.

65. Palik, E. D., *Handbook of optical constants of solids*, Academic press, San Diego, 1998.

66. Cardenas, J. F., "Modelling the spectral selective solar absorption properties of graphite–silica composite/aluminium structures", *Thin Solid Films*, Vol. 586, pp. 76–81, 07 2015.

67. Hale, M. R., George M.and Querry, "Optical Constants of Water in the 200-nm to 200-μm Wavelength Region", *Applied Optics*, Vol. 12, pp. 555–563, 1973.

68. Sani, E. and A. Dell'Oro, "Optical constants of ethylene glycol over an extremely wide spectral range", *Optical Materials*, Vol. 37, pp. 36–41, 11 2014.

69. Rubin, M., "Optical properties of soda lime silica glasses", *Solar Energy Materials*, Vol. 12, pp. 275–288, 1985.

70. Veeraragavan, A., A. Lenert, B. Yilbas, S. Al-Dini, and E. N. Wang, "Analytical

model for the design of volumetric solar flow receivers", *International Journal of Heat and Mass Transfer*, Vol. 55, No. 4, pp. 556–564, 2012.

71. Rohsenow, W., J. Hartnett, and Y. Cho, *Handbook of Heat Transfer*, McGraw-Hill, New York, 3rd edition, 1998.

72. Chawla, S. H., T. C.and Chan, "Combined Radiation Convection in Thermally Developing Poiseuille Flow with Scattering", *Journal of Heat Transfer*, Vol. 102, pp. 297–302, 1980.

73. Streed, E. R., J. E. Hill, W. C. Thomas, A. G. Dawson, and B. D. Wood, "Results and analysis of a round robin test program for liquid-heating flat-plate solar collectors", *Solar Energy*, Vol. 22, No. 3, pp. 235–249, 1979.

APPENDIX A: RESULTS FOR THE FLAT PLATE COLLECTOR

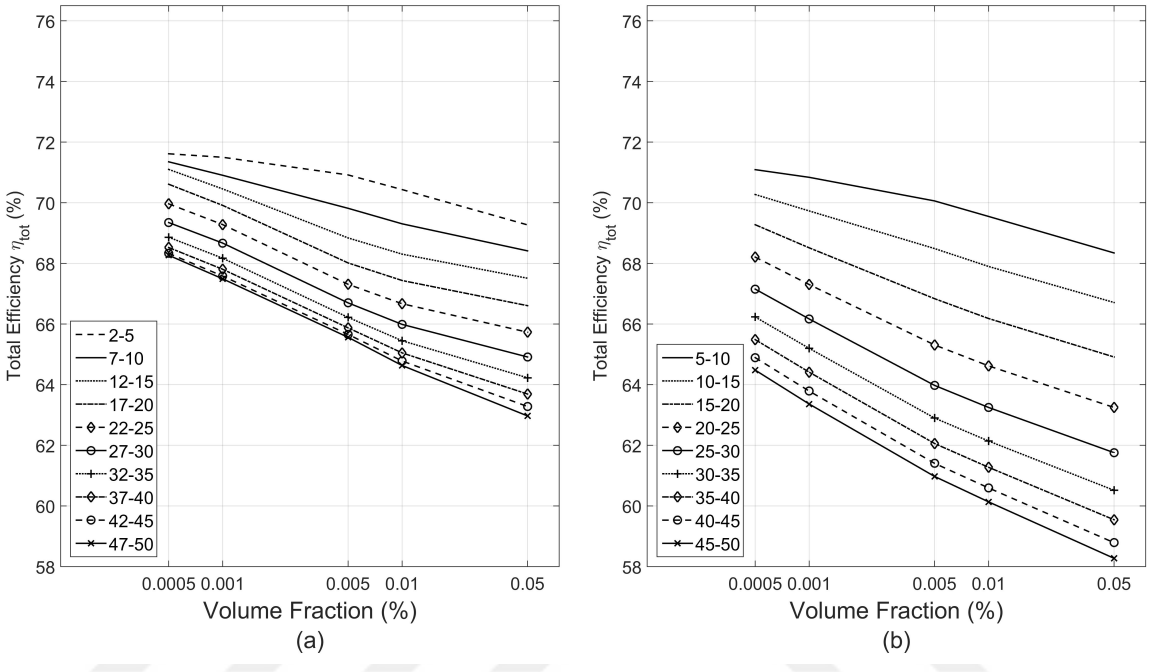

Figure A.1. Total efficiency results for EG SiO_2-Ag nanofluid with shell thickness (a) 3 nm (b) 5 nm.

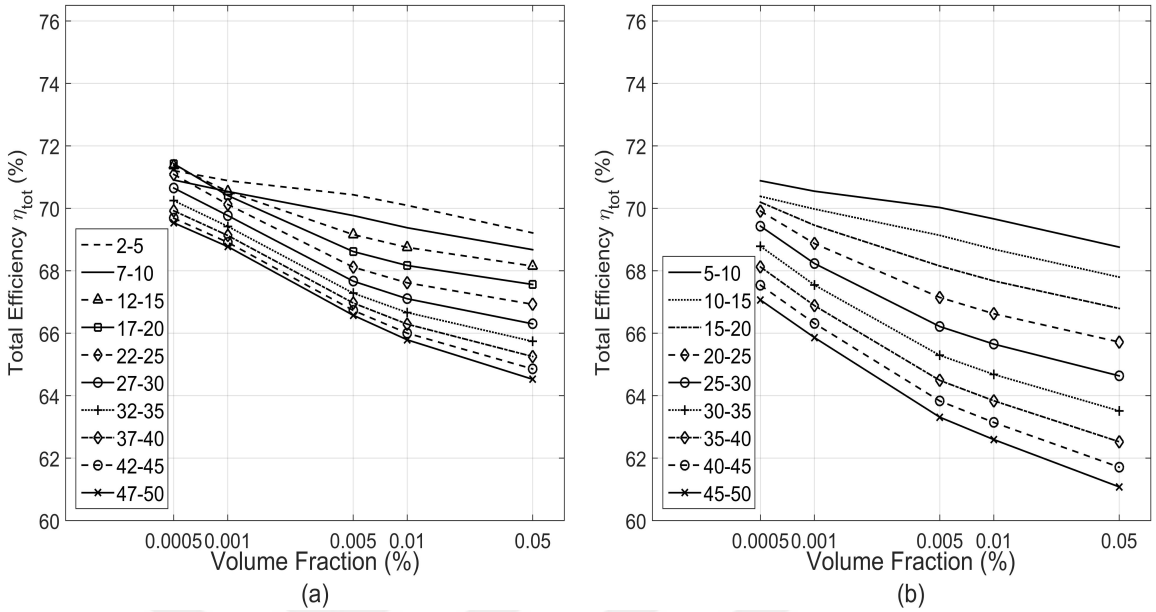

Figure A.2. Total efficiency results for EG SiO_2-Au nanofluid with shell thickness (a) 3 nm (b) 5 nm.

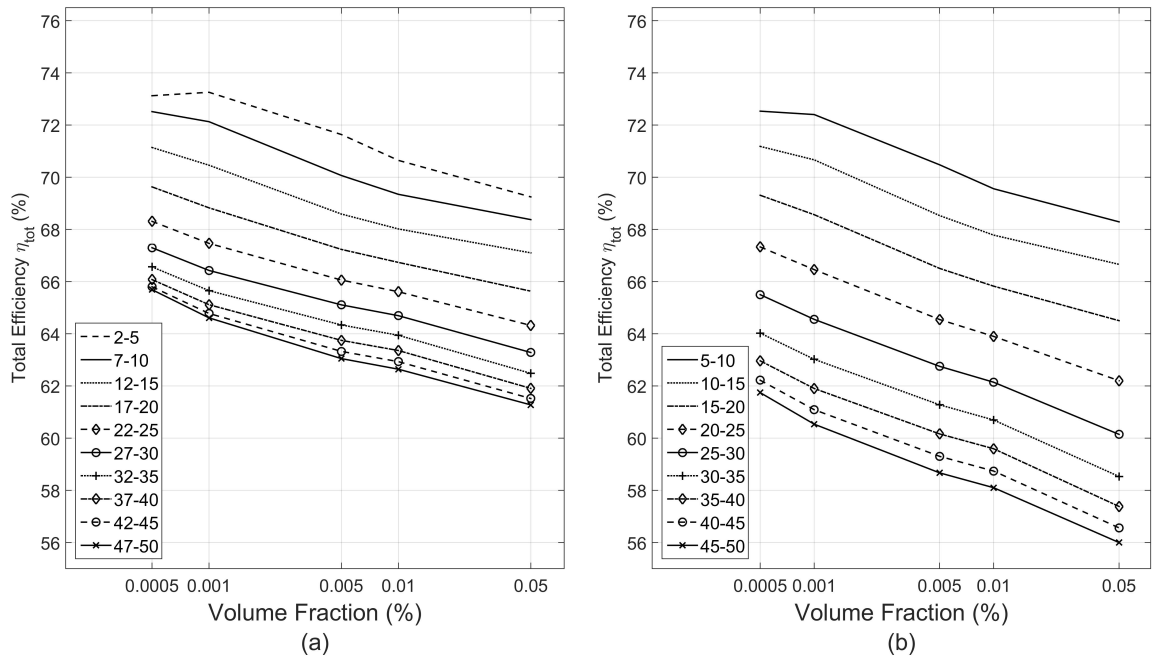

Figure A.3. Total efficiency results for EG SiO_2-Al nanofluid with shell thickness (a) 3 nm (b) 5 nm.

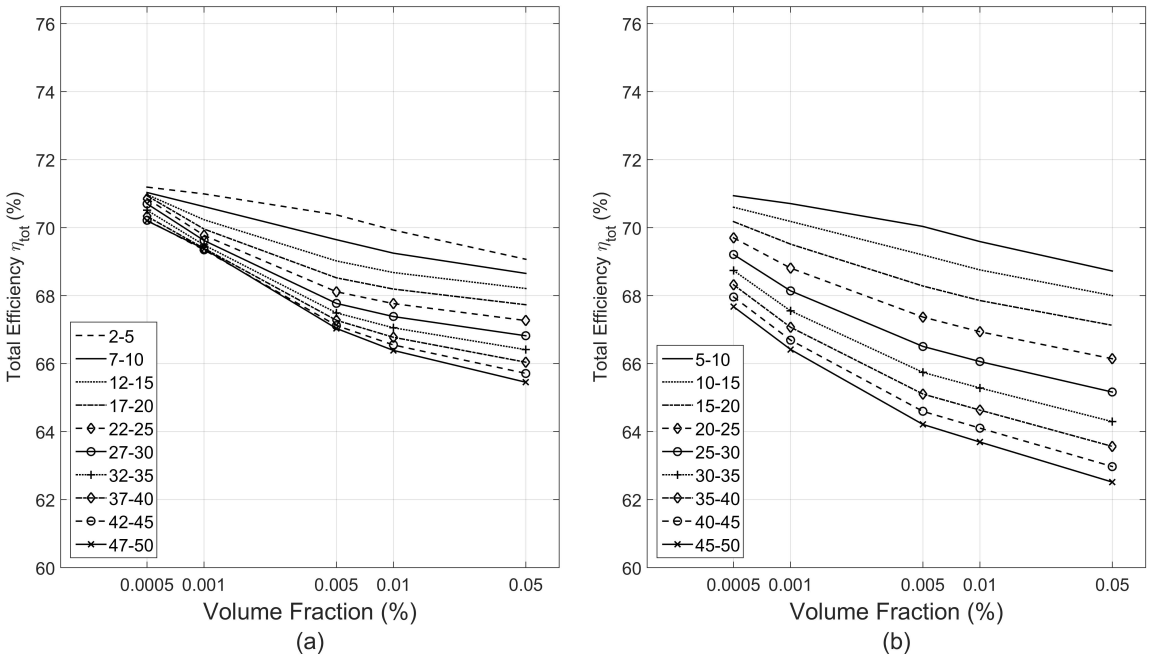

Figure A.4. Total efficiency results for EG SiO_2-Cu nanofluid with shell thickness (a) 3 nm (b) 5 nm.

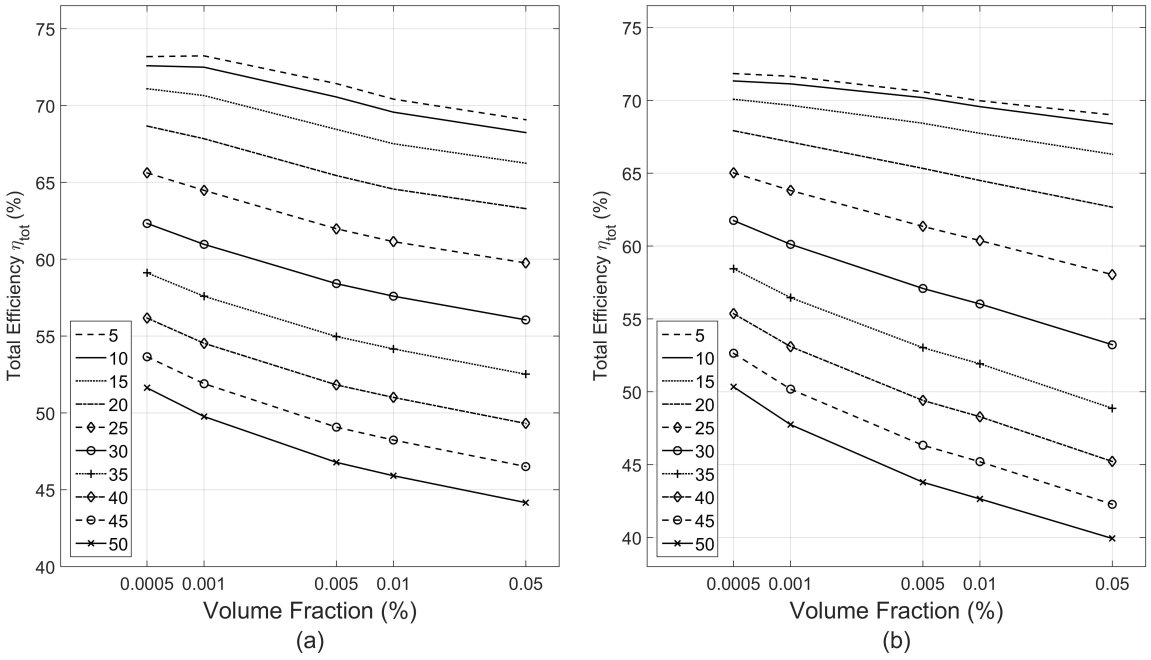

Figure A.5. Total efficiency results for (a) Al (b) Ag nanoparticles in EG.

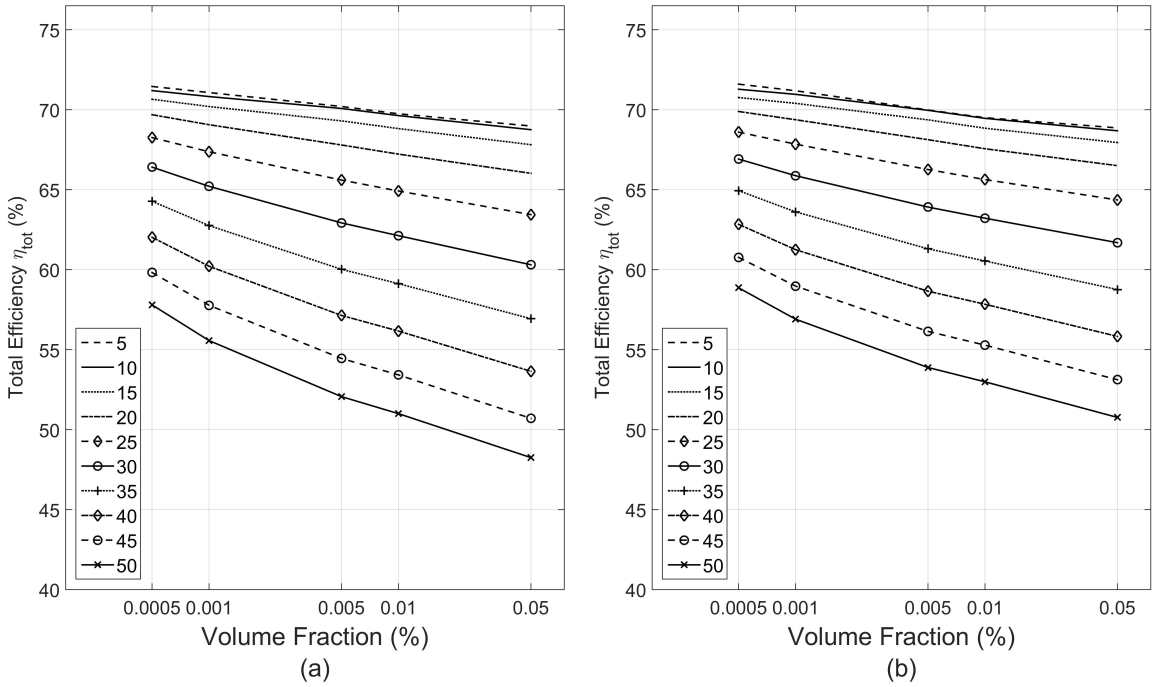

Figure A.6. Total efficiency results for (a) Au (b) Cu nanoparticles in EG.

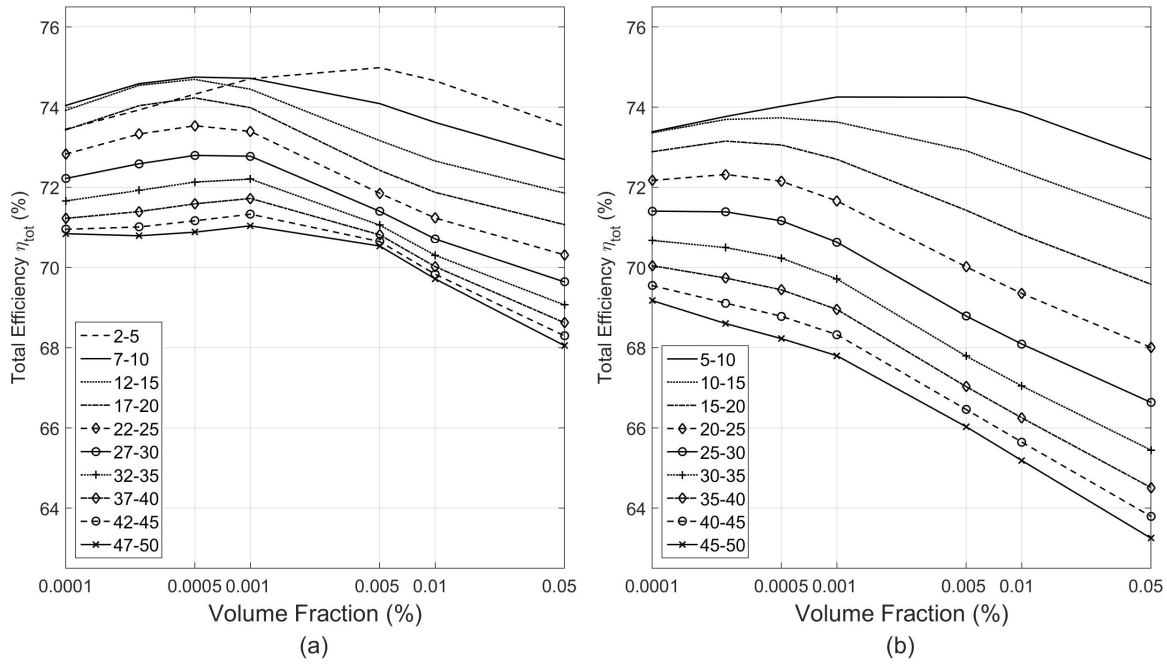

Figure A.7. Total efficiency results for water SiO_2-Ag nanofluid with shell thickness (a) 3 nm (b) 5 nm.

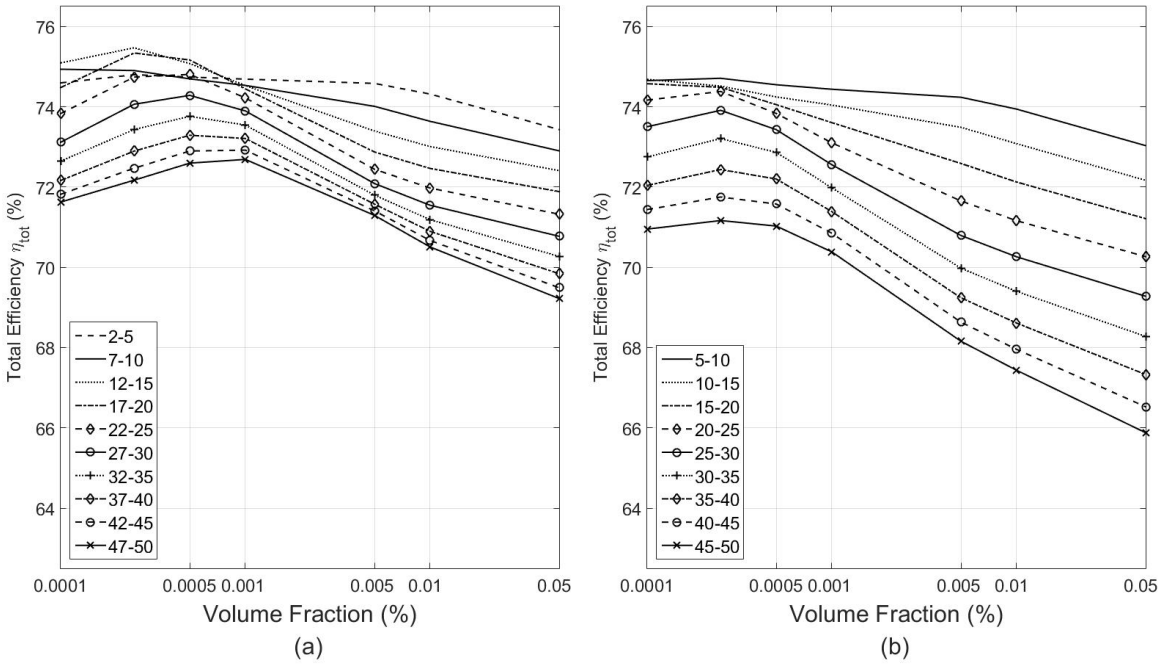

Figure A.8. Total efficiency results for water SiO_2-Au nanofluid with shell thickness (a) 3 nm (b) 5 nm.

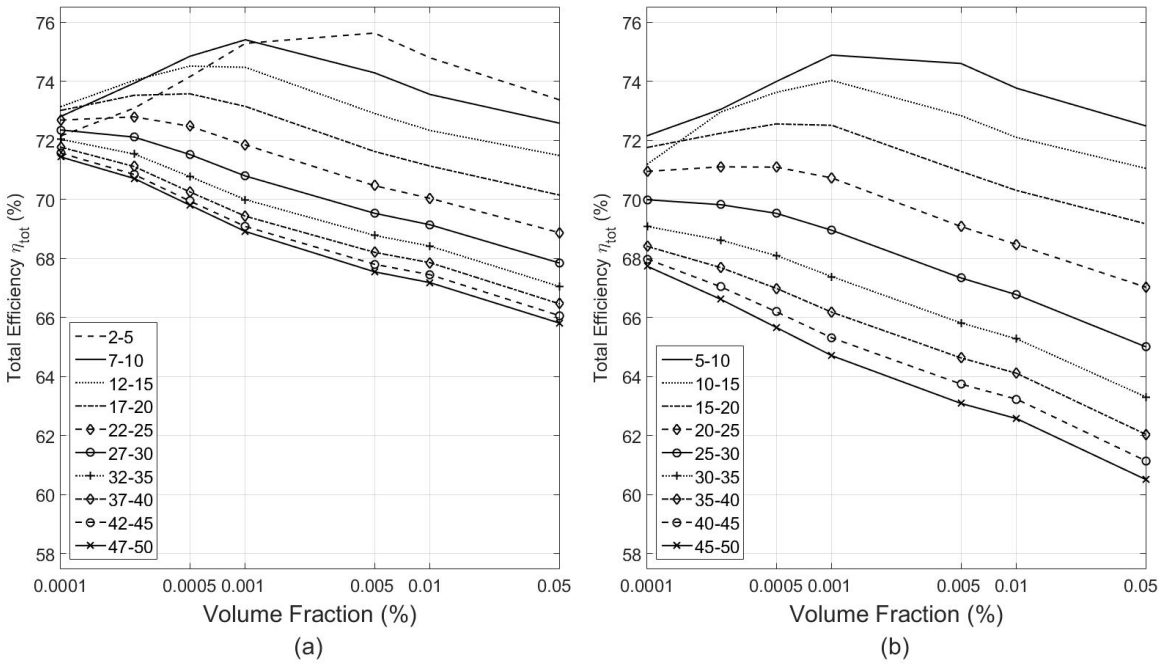

Figure A.9. Total efficiency results for water SiO_2-Al nanofluid with shell thickness (a) 3 nm (b) 5 nm.

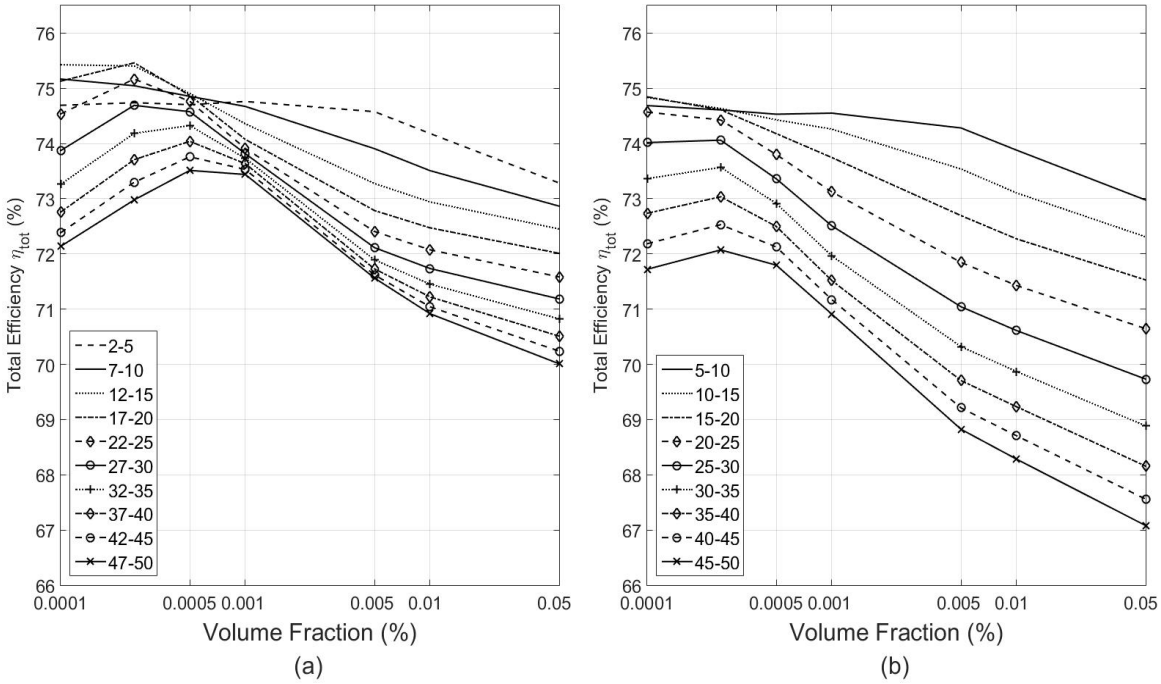

Figure A.10. Total efficiency results for water SiO_2-Cu nanofluid with shell thickness (a) 3 nm (b) 5 nm.

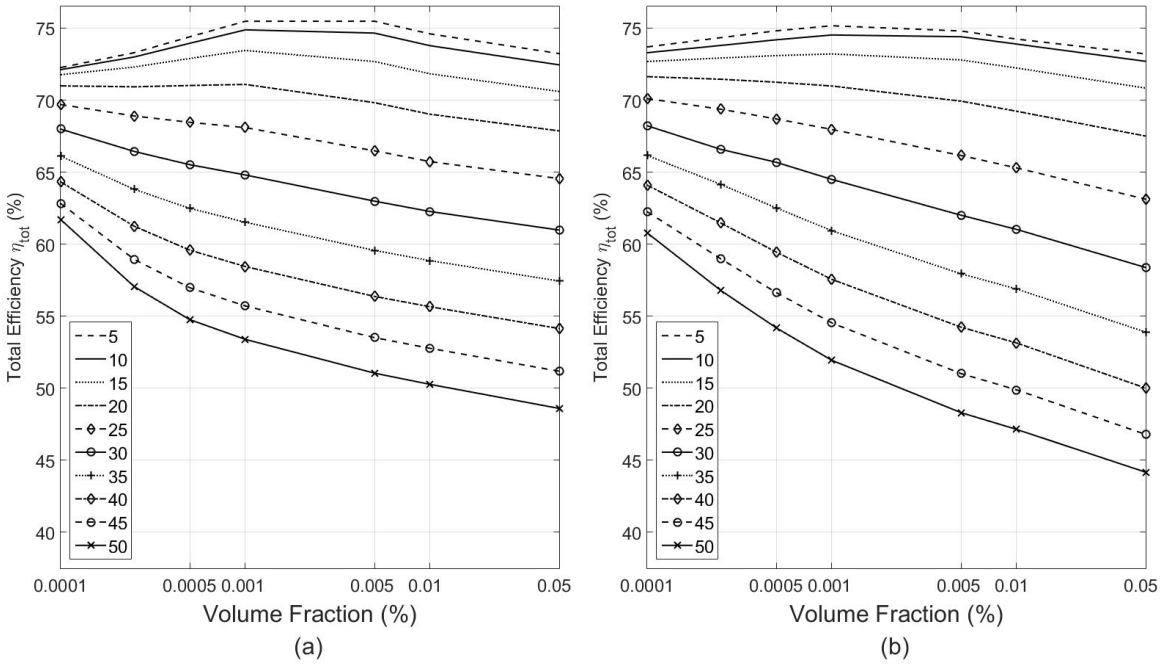

Figure A.11. Total efficiency results for (a) Al (b) Ag nanoparticles in water.

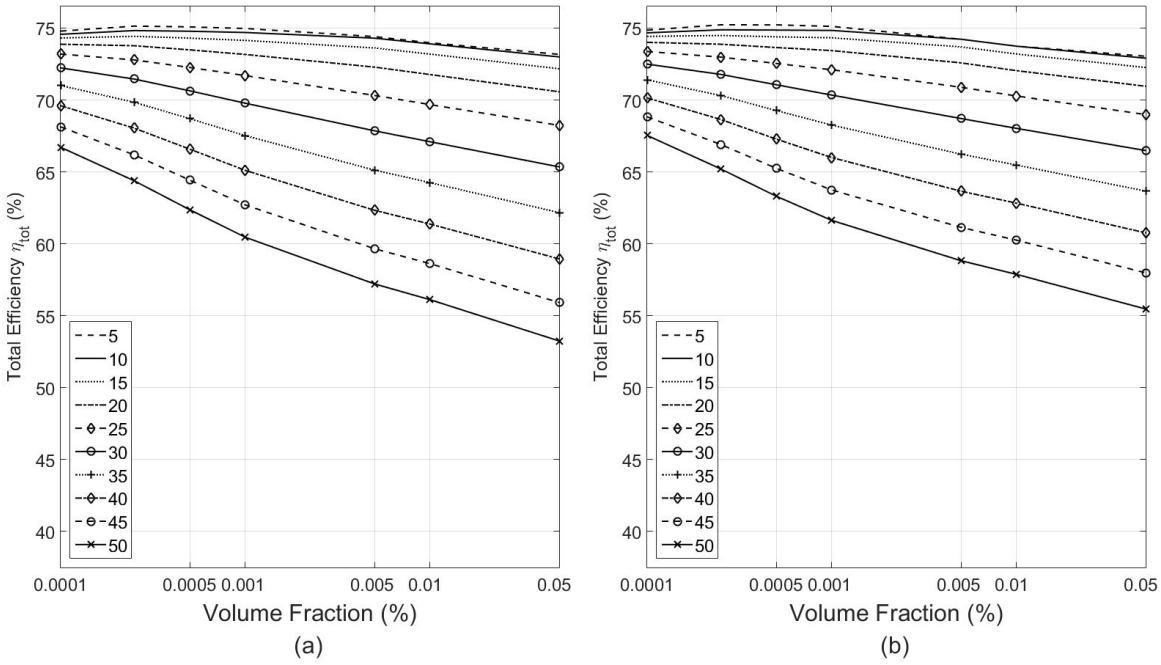

Figure A.12. Total efficiency results for (a) Au (b) Cu nanoparticles in water.

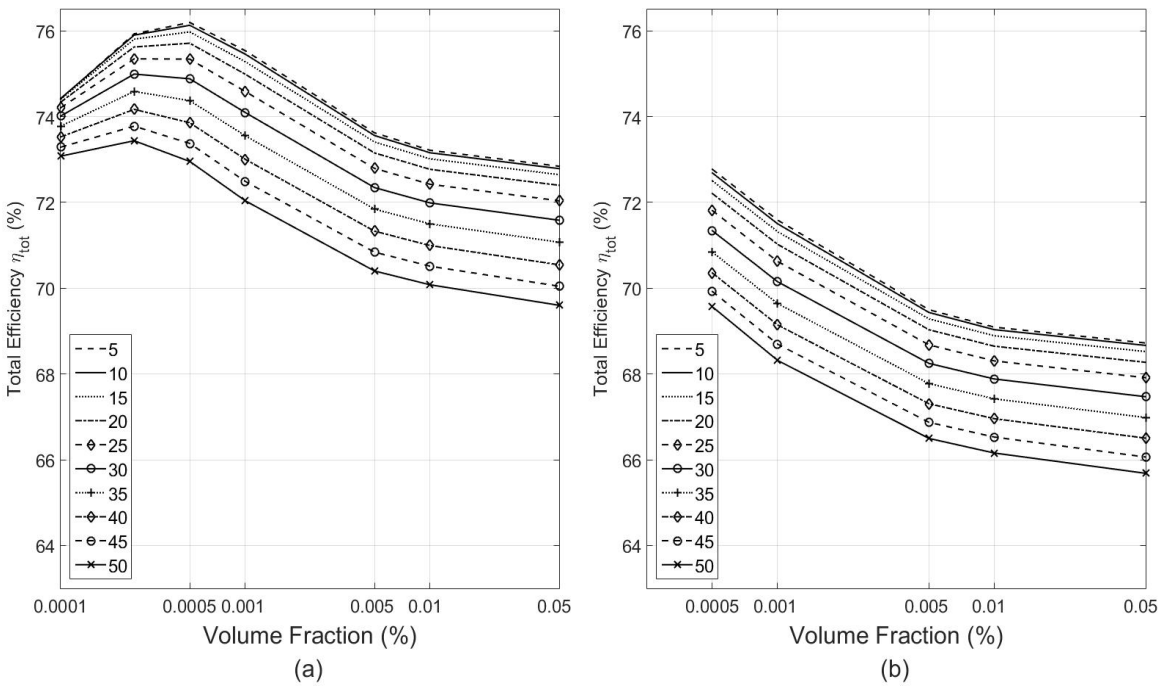

Figure A.13. Total efficiency results for graphite nanoparticles in (a) water (b) EG.